Charles University Prague
Faculty of Mathematics and Physics

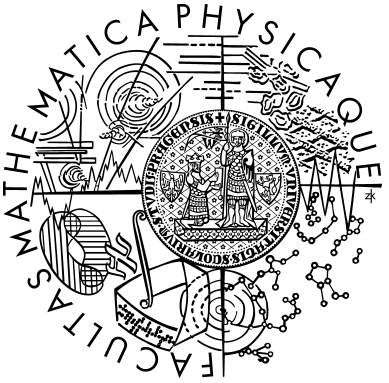

Solar wind discontinuities and their interaction with the bow shock

Doctoral thesis in branch F-2,
Physics of Plasma and Ionized Media

Andriy Koval

Thesis supervisor: Prof. RNDr. Jana Šafránková, DrSc.
Department of Electronics and Vacuum Physics

Prague 2006

Contents

Preface

The speed and geometry of a shock that precedes ejecta from a solar energetic eruption is one of the key parameters used for input by many numerical models that predict the arrival of interplanetary shocks at the Earth. These shocks are likely to be followed by a significant geomagnetic activity. It is a reason for the main topic of this thesis — the propagation of solar wind origin instabilities in the solar wind and in the magnetosheath.

The thesis is arranged as follows. After the introduction where our present knowledge of solar wind discontinuities is summarized, Chapter 2 presents the aims of the thesis. Chapter 3 describes spacecraft measurements in the solar wind and magnetosheath and new methods of plasma parameter determination. In Chapter 4, these methods are applied for the analysis of particle flows in hot flow anomalies. Chapter 5 contains a study of interplanetary shock propagation through the solar wind and magnetosheath, including comparison of observations with MHD models. Finally, Chapter 6 summarizes the conclusions of the thesis.

The present work was supported by the Czech Grant Agency under Contracts *No.* 205/02/0947, 205/03/0953, 202/03/H162, 205/05/0170, by the Czech Ministry of Education grant ME-648, by the Research Projects of the Czech Ministry of Education MSM 113200004, by the INTAS grant for young scientists 03-55-1034, by the RFBR grant 03-05-64865, and by the USA NSF grants ATM-0207775 and ATM-0203723.

Acknowledgments

I am grateful to my thesis supervisor Prof. RNDr. Jana Šafránková, DrSc. and to Prof. RNDr. Zdeněk Němeček, DrSc. for their continuous help during the whole graduate study and the thesis preparation. I also appreciate Doc. RNDr. Lubomír Přech, Dr. for his valuable advices in programming and data processing.

Chapter 1

Introduction

1.1 The solar wind and the Earth's magnetosphere

1.1.1 The solar wind and the interplanetary magnetic field

The solar wind

The solar wind (SW) is a flow of ionized solar plasma and a remnant of the solar magnetic field that pervades interplanetary space. The existence of a solar wind was surmised in the 1950s on the basis of evidence that small variations in the Earth's magnetic field were produced by observable phenomena on the Sun. *Parker* (1958) predicted continuous, supersonic flow of plasma from the corona into an interplanetary medium based upon a hydrodynamic model for the equilibrium state of the solar corona. Figure 1.1 shows the results of an isothermal hydrodynamic treatment of the supersonic expansion from the corona as described by *Parker* (1958). As Figure 1.1 illustrates, the solar wind achieves close to its asymptotic velocity by the time it reaches the orbit of the Earth, one astronomical unit (AU) or about 1.5×10^8 km from the Sun.

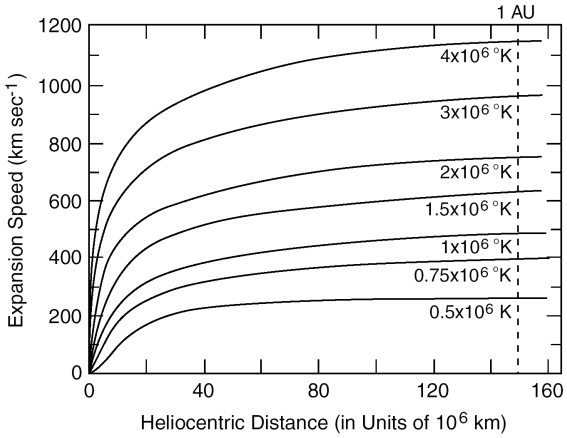

Figure 1.1: Theoretically derived speed of the solar wind from an isothermal model for varying coronal temperatures. Adapted from *Parker* (1958).

The existence of the solar wind was first observed directly and definitively by space

probes in mid-1960s. Measurements taken by spacecraft-born instruments since that time have yielded a detailed description of the solar wind across an area from inside the orbit of Mercury to well beyond the orbit of Saturn. The most extensive and most detailed observations of the solar wind have been made from the spacecraft near the orbit of the Earth. Some of the physical properties of the plasma and magnetic field at this distance from the Sun are summarized in Table 1.1. The solar wind consists largely of ionized hydrogen (or protons and electrons in nearly equal numbers), with a small (5% by number) admixture of ionized helium and still fewer ions of heavier elements.

Proton density	6.6 cm^{-3}
Electron density	7.1 cm^{-3}
He^{2+} density	0.25 cm^{-3}
Flow speed	450 km s^{-1}
Proton temperature	1.2×10^5 K
Electron temperature	1.4×10^5 K
Magnetic field	7×10^{-9} T

Table 1.1: Average values of the solar wind parameters observed near the orbit of the Earth. Adapted from *Hundhausen* (1993).

Although frequently it is possible to treat ions as a single fluid in the solar wind, this is not true for electrons. Electrons most frequently appear to have at least two components, a core and a halo. As shown in Figure 1.2, the core is colder than the halo and it is denser.

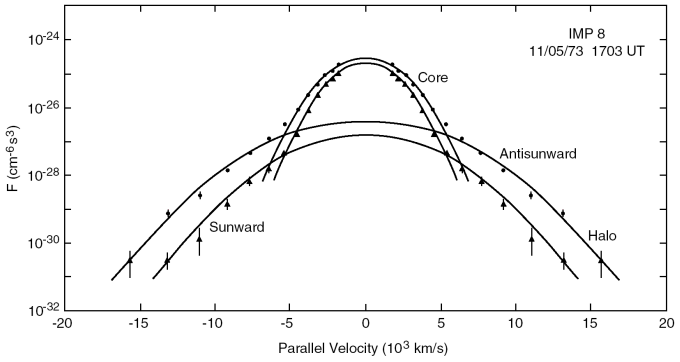

Figure 1.2: The distribution function of solar wind electrons along the magnetic field direction showing the core and halo populations and their differing bulk velocities and temperatures. Adapted from *Feldman et al.* (1975).

At the orbit of the Earth, the solar wind is highly variable. The left panel of Figure 1.3 shows a histogram of the solar wind velocity. It can be as slow as 260 km s^{-1} and faster than 750 km s^{-1}, however, typically lies about 400 km s^{-1}. The density, shown in the right panel of Figure 1.3, is much more variable than the velocity, ranging from about 0.1 cm^{-3} to 100 cm^{-3}. These variations in density and solar wind velocity are, in general, inversely correlated as shown in Figure 1.4. On the other hand, the ion temperature is positively correlated with the solar wind velocity as shown in the left panel of Figure 1.5. This correlation is certainly qualitatively consistent with the Parker's model of solar wind expansion illustrated in Figure 1.1. In stark contrast to the ions, the electrons have a nearly

constant temperature when averaged over the distribution function which is dominated by the denser core electrons. The right panel of Figure 1.5 demonstrates this constancy versus the solar wind velocity.

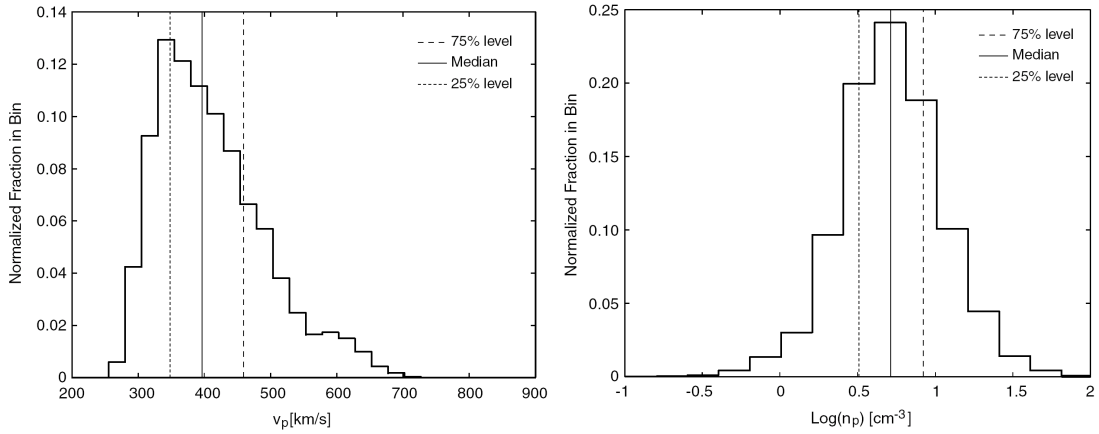

Figure 1.3: Histogram of the solar wind velocity (*left*) and density (*right*) derived from 18 months of ISEE-3 observations. Quartiles of the velocity are: 348, 397 and 459 km s^{-1}. Quartiles of the density are: 3.2, 5.2 and 8.4 cm^{-3}. Adapted from *Newbury* (2000).

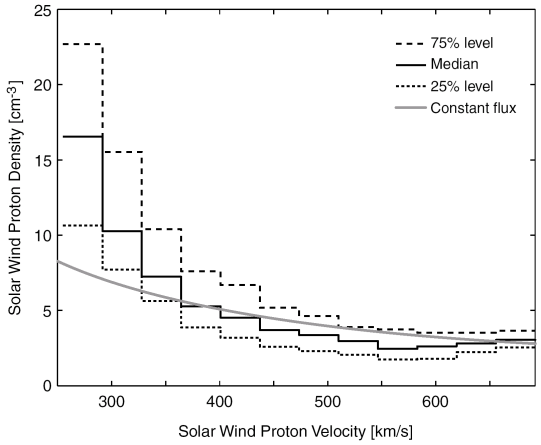

Figure 1.4: The variation of the solar wind density as a function of the solar wind velocity. The median, quartiles and the line of constant flux are shown. Adapted from *Newbury* (2000).

The solar wind properties are non uniform and highly depend on heliolatitude. Figure 1.6 shows the solar wind speed and magnetic field polarity measured by Ulysses as a function of heliolatitude (*McComas et al.*, 1998b). The polar regions correspond to high solar wind speed and low density while the equatorial regions correspond to slow, relatively dense solar wind.

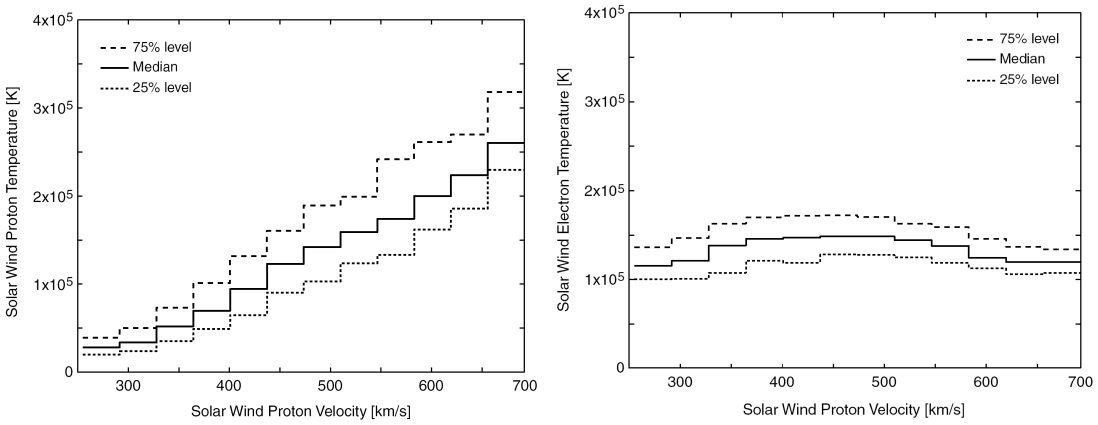

Figure 1.5: Variations of the solar wind proton (*left*) and electron (*right*) temperatures with the solar wind velocity. Medians and quartiles are shown. Adapted from *Newbury* (2000).

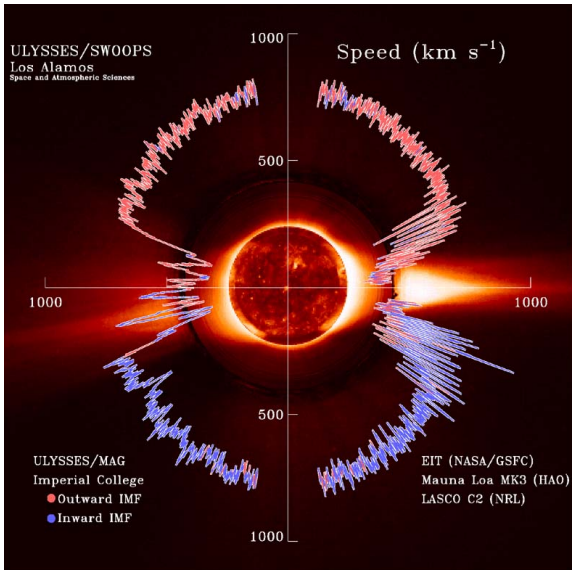

Figure 1.6: Solar wind speed and the sense of the magnetic field's radial component measured by Ulysses as a function of heliolatitude. Adapted from *McComas et al.* (1998b).

The interplanetary magnetic field

The solar magnetic field embedded in the plasma is carried into a space by the solar wind to form the interplanetary magnetic field (IMF). Because of solar rotation, the point where the open field line is anchored to the Sun moves and as a result, the interplanetary magnetic field has the form of a spiral. At the orbit of the Earth, the interplanetary magnetic field makes an angle of about 45° to the radial direction. Further out, the field is nearly transverse (i.e., about 90°) to the radial direction. Figure 1.7 shows this spiral geometry for a constant solar wind speed of 400 km s^{-1}.

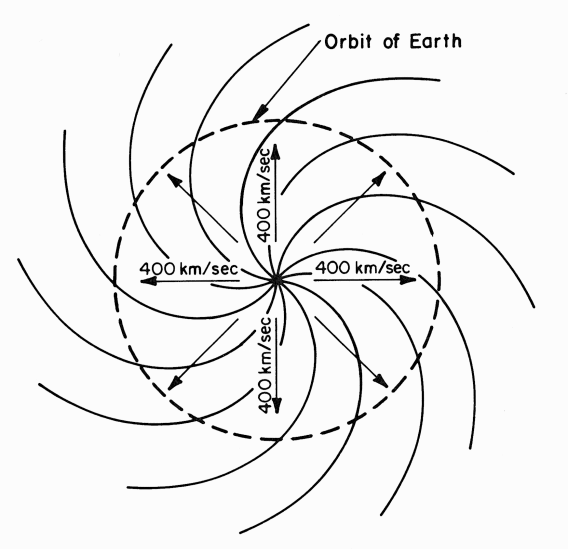

Figure 1.7: Spiral interplanetary magnetic field lines frozen into a radial solar wind expansion at 400 km s^{-1}. Adapted from *Parker* (1963).

The magnetic patterns are usually not dipolar and, moreover, they are often not symmetric with respect to the Sun's rotation axis. Thus, as the Sun rotates, the pattern set by the Sun's field sweeps over the Earth causing magnetic sectors seen in the interplanetary magnetic field as it is illustrated in a 3-D perspective in Figure 1.8. Furthermore, the Earth's orbit is not in the rotational equator of the Sun so that in the course of a year, the Earth spends six months above the rotational equator and six month below it. Since the solar wind properties also depend on heliolatitude, as shown in Figure 1.6, these IMF variations are accompanied with variations in the solar wind properties.

1.1.2 Interaction of the solar wind with the Earth's magnetosphere

The Earth has an internal dipole magnetic moment of 8×10^{15} Tm^3 that produces a magnetic field strength at the equator on the Earth's surface of about 30×10^3 nT, and at 10 Earth radii (R_E or 6378 km) of about 30 nT. The solar wind interaction slightly more than doubles this value on the dayside, so that the pressure in the magnetic field is about 2 nPa. The pressure exerted by the solar wind plasma is also about 2 nPa, thus balancing the pressure exerted by the magnetospheric field.

The variations in the dynamic pressure of the solar wind and hence the size of the magnetosphere are controlled principally by density fluctuations. The factor of three

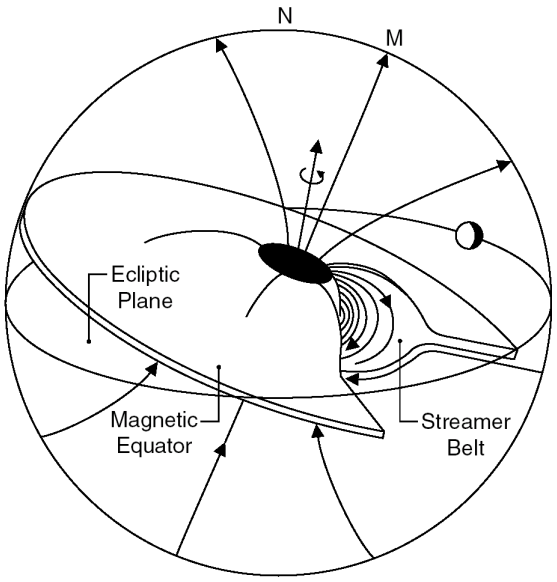

Figure 1.8: Idealized three dimensional view of the streamer belt and the coronal magnetic field. Orbit of the Earth carries it above and below the Suns equator in the course of the year. Because the streamer belt is tilted with respect to the rotational equator the streamer belt can sweep across the Earth twice every solar rotation. Adapted from *Hundhausen* (1977).

changes in the velocity (left panel in Figure 1.3) makes a $\pm$20% change in the radius of the magnetosphere but the range of density (right panel in Figure 1.3) makes a $\pm$80% change. Over the solar cycle, the yearly averaged dynamic pressure changes about $\pm$20% (*Petrinec et al.*, 1991). This makes a small but perceptible ($\pm$3%) change in the size of the magnetosphere. When high densities and high velocities occur together, the size of the magnetosphere can be halved but, in general, the density of the solar wind and the velocity are inversely correlated as shown in Figure 1.4.

Three types of waves propagate in the magnetized solar wind plasma. They are ordered by their speeds, which are called fast, intermediate, and slow (V_F, V_I, V_{SL}, respectively). The fast mode wave compresses the magnetic field and plasma; the intermediate mode wave bends the flow and magnetic field but does not compress it; and the slow mode wave rarefies the field while it compresses the plasma and vice versa.

The speeds of the waves depend upon the angle θ of their propagation to the magnetic field, $\boldsymbol{B}$, and sound and Alfvén speeds, V_S and V_A, respectively:

$$V_I = \sqrt{V_A^2 \cos^2\theta} \tag{1.1}$$

$$\begin{matrix} V_F \\ V_{SL} \end{matrix} = \sqrt{\frac{1}{2}\left\{(V_A^2 + V_S^2) \pm [(V_A^2 + V_S^2)^2 - 4\,V_A^2\,V_S^2\cos^2\theta]^{\frac{1}{2}}\right\}} \tag{1.2}$$

where

$$V_S = \sqrt{\frac{\gamma P}{\rho}}, \quad V_A = \frac{B}{\sqrt{\mu_0 \rho}} \tag{1.3}$$

and P, ρ, and γ are the plasma pressure, mass density, and the ratio of specific heats. By defining the fast mode to have the larger of two speeds in equation (1.2), it follows that $V_F \geq V_I \geq V_{SL}$ for all θ, V_S, and V_A.

For propagating perpendicular to the magnetic field (θ=90°), equations (1.1) and (1.2) reduce to

$$V_I = V_{SL} = 0, \quad V_F = \sqrt{(V_A^2 + V_S^2)} \equiv V_{MS} \tag{1.4}$$

so that only one wave, the magnetosonic wave, propagates with a nonzero speed. For parallel propagation (θ=0°), equations (1.1) and (1.2) indicate that when $V_A > V_S$, the fast and intermediate speeds are identical, whereas when $V_S > V_A$, the intermediate and slow speeds are equal. For all other angles of propagation, three magnetohydrodynamic (MHD) speeds are distinct.

It is convenient to characterize the solar wind speed in terms of slow, intermediate, and fast Mach numbers which are the ratios of the solar wind velocity to the corresponding wave speed:

$$M_{SL} = \frac{V_{sw}}{V_{SL}}, \quad M_I = \frac{V_{sw}}{V_I}, \quad M_F = \frac{V_{sw}}{V_F}. \tag{1.5}$$

The solar wind speed is also often represented by the Alfvén Mach number, since it does not depend on the θ angle:

$$M_A = \frac{V_{sw}}{V_A}. \tag{1.6}$$

The solar wind travels faster than the propagation speed of all three of these waves ($M_{SL} > 1, M_I > 1, M_F > 1$), so when it reaches the Earth's magnetosphere the "pressure" waves needed to deflect the solar wind plasma cannot propagate upstream into the solar wind without creating a shock front. The geometry of this shock, the deflected flow, called the magnetosheath, and the magnetopause, the boundary between the magnetosheath and the magnetosphere, are shown in Figure 1.9. The side from where the undisturbed solar wind flows into the bow shock is called upstream side, whereas the opposite side is called the downstream side. The fast mode wave does the work in slowing, deflecting, and heating the solar wind downstream of the bow shock so that the plasma can flow around the magnetosphere. Nevertheless, it cannot cause all of the changes in the plasma needed to move both plasma and the magnetic field around the bullet-shaped magnetosphere. Thus, the intermediate and slow modes also play roles. The net result of these waves is a flow that moves parallel to the magnetopause.

The properties of the magnetosheath significantly differ from the upstream solar wind. Near the nose of the bow shock, the magnetosheath plasma is primarily a hot, dense, slow plasma with $T_i \gg T_e$. However, this flow accelerates up towards the solar wind speed and becomes increasingly solar wind-like towards the flanks of the bow shock, as the shock becomes increasingly weak. For instance, Figure 1.10 shows the spatially-varying characteristics of the magnetosheath plasma from the gas-dynamic model of *Spreiter et al.* (1966).

1.2 Solar wind discontinuities

In addition to the recurrent variations in the solar-wind properties described in Section 1.1.1, there are sporadic disturbances that involve true time variations. Among them, solar wind

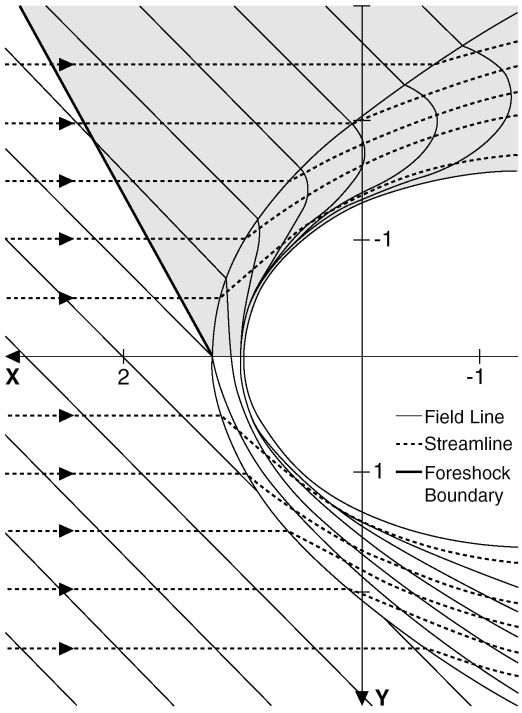

Figure 1.9: The magnetic field and the solar wind flow as they encounter the Earth's bow shock and the magnetosphere according to the gas-dynamic model (*Spreiter et al.*, 1966). The plane of the figure contains the magnetic field lines and the streamlines that are carried to the subsolar point. In the shaded region, energetic ions accelerated at the shock can move upstream. Adapted from *Spreiter et al.* (1966).

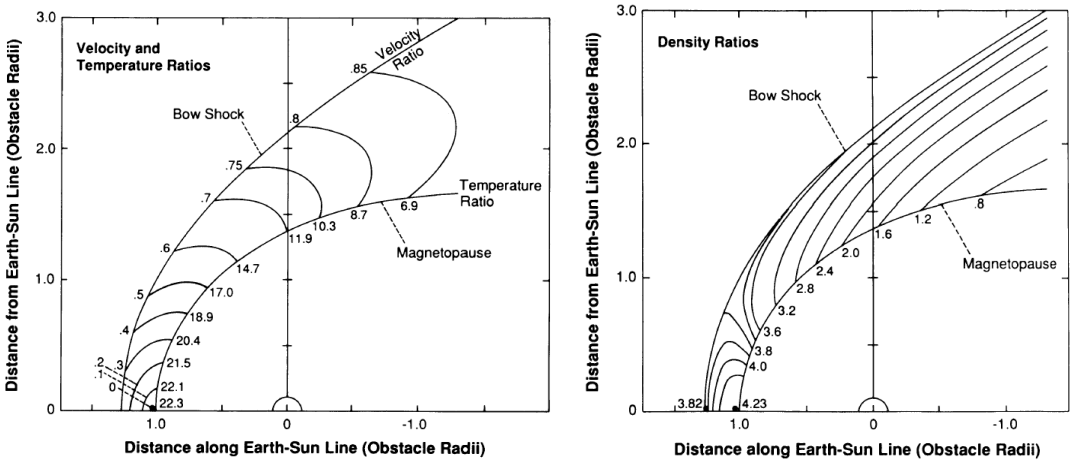

Figure 1.10: Contours of the plasma velocity and temperature (*left*), and density (*right*) in the magnetosheath normalized to upstream solar wind values. Adapted from *Spreiter et al.* (1966).

discontinuities, including interplanetary shocks, are of a special interest. These discontinuities, detected by abrupt changes in the magnetic field and plasma parameters, are common features of the solar wind. As an example, Figure 1.11 shows solar wind properties observed by Wind during December 10, 1997. It can be seen that there are many discontinuities with different characteristics. Two of them, observed at about 0430 UT and 1830 UT, can be classified as interplanetary shocks as we will show later.

The geocentric solar ecliptic (GSE) coordinate system used here and hereafter is defined as follows: its X-axis points from the Earth towards the Sun; the Y-axis is chosen to be in the ecliptic plane pointing towards dusk (thus opposing planetary motion), and the Z-axis makes up the right-handed set.

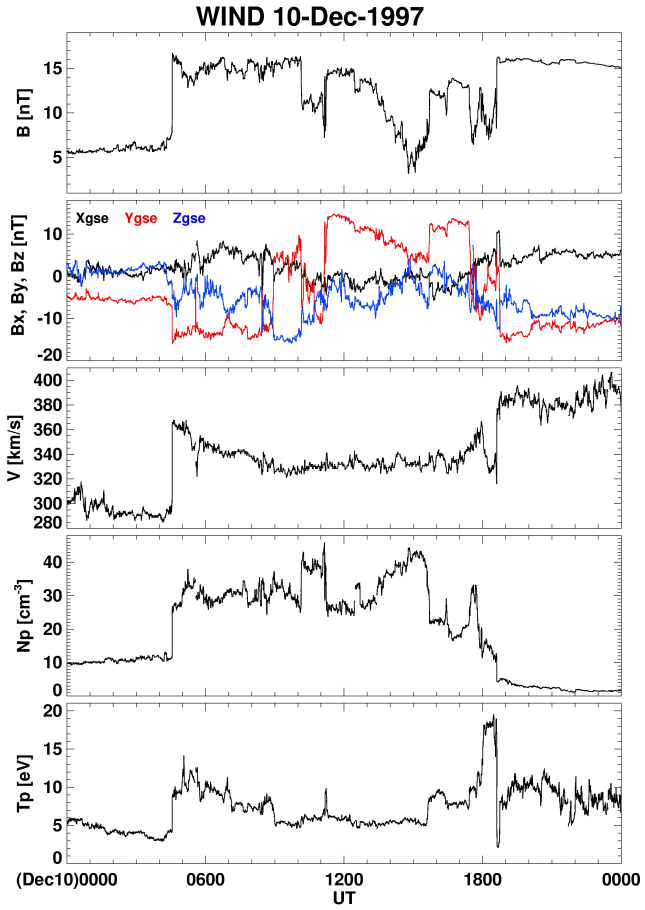

Figure 1.11: Magnetic field magnitude (B) and components (Bx, By, Bz) in GSE coordinates, solar wind velocity (V), proton number density (Np), and temperature (Tp) observed by Wind on December 10, 1997.

1.2.1 Conservation relations across a discontinuity

At the macroscopic level, a discontinuity must conserve total mass, momentum and energy fluxes, together with a normal component of the magnetic field and a tangential

component of the electric field (*Landau and Lifshitz*, 1960). Since all measurements of the solar wind properties are made by the spacecraft, it is convenient to represent the conservation relations, called Rankine-Hugoniot (RH) conservation equations, in a spacecraft frame of reference. These equations for isotropic scalar pressures and an assumed polytropic equation of state are (e.g., according to *Szabo*, 1994):

$$\Delta[G_n] \equiv \Delta[\rho\,(V_n - V_d)] = 0 \tag{1.7}$$

$$\Delta[B_n] \equiv \Delta[\boldsymbol{B}\cdot\boldsymbol{n}] = 0 \tag{1.8}$$

$$\Delta[\boldsymbol{S}_t] \equiv \Delta\left[\rho\,(V_n - V_d)\,\boldsymbol{V}_t - \frac{B_n}{\mu_0}\,\boldsymbol{B}_t\right] = 0 \tag{1.9}$$

$$\Delta[\boldsymbol{E}_t] \equiv \Delta[(\boldsymbol{n}\times\boldsymbol{V}_t)\,B_n - (V_n - V_d)(\boldsymbol{n}\times\boldsymbol{B}_t)] = 0 \tag{1.10}$$

$$\Delta[S_n] \equiv \Delta\left[P + \frac{B_t^2}{2\mu_0} + \rho\,(V_n - V_d)^2\right] = 0 \tag{1.11}$$

$$\Delta[\varepsilon] \equiv \Delta\left[\rho\,(V_n - V_d)\left(\frac{(\boldsymbol{V} - V_d\,\boldsymbol{n})^2}{2} + \frac{\gamma}{\gamma-1}\frac{P}{\rho} + \frac{B^2}{\mu_0\rho}\right) - \frac{B_n\,(\boldsymbol{V} - V_d\,\boldsymbol{n})\,\boldsymbol{B}}{\mu_0}\right] = 0 \tag{1.12}$$

where ρ is the mass density, $\boldsymbol{V}$ is the plasma bulk velocity, $\boldsymbol{B}$ is the magnetic field, $\boldsymbol{n}$ is the discontinuity unit normal, V_d is the discontinuity speed relative to the flow in the normal direction, $P = nkT$ is the total scalar isotropic thermal pressure, γ is the ratio of the specific heats, and μ_0 is the permeability of vacuum. The subscripts n and t refer to the components normal and tangential to the discontinuity surface. The variables G_n, B_n, $\boldsymbol{S}_t$, $\boldsymbol{E}_t$, S_n, and ε represent the conservation constants corresponding to the mass flux, normal magnetic field, tangential momentum flux (stress), tangential electric field, normal momentum flux, and energy flux, respectively. The notation $\Delta[\ ]$ is applied as a difference across the discontinuity.

Since equations (1.9) and (1.10) are two-dimensional vector equations, equations (1.7) through (1.12) represent eight independent equations. If the discontinuity normal $\boldsymbol{n}$ and speed V_d are known, there are eight unknowns (ρ, V_n, $\boldsymbol{V}_t$, P, B_n, $\boldsymbol{B}_t$), and therefore, the downstream state can be specified uniquely in terms of the upstream state. However, in the case of an anisotropic pressure (e.g., pressures parallel and perpendicular to the magnetic field are different) or a more complicated system (e.g., two-fluid or multi-species environment), there are in general fewer equations than parameters. In such cases, additional relations from theory or observations are required to close the system.

The solution of these equations describes a number of different types of MHD discontinuities (including shocks) which are summarized in Table 1.2 and discussed in the following sections.

Contact discontinuity	$V_n = 0, B_n \neq 0$	Density jump arbitrary, but pressure and all other quantities are continuous
Tangential discontinuity	$V_n = 0, B_n = 0$	Plasma pressure and field change, maintaining static pressure balance
Rotational discontinuity	$V_n = B_n/\sqrt{\mu_0 \rho}$	Large-amplitude intermediate wave; in isotropic plasma, field and flow change directions, but not magnitude
Shock waves	$V_n \neq 0$	Flow crosses surface of discontinuity accompanied by compression and dissipation
Fast shock		Plasma pressure and field strength increase at shock; magnetic field bends away from normal
Slow shock		Plasma pressure increases; magnetic filed strength decreases; magnetic filed bends toward normal
Intermediate shock		Magnetic filed rotation of 180° in plane of shock; density jump only in anisotropic plasma
Parallel shock	$B_t = 0$	Magnetic field unchanged by shock
Perpendicular shock	$B_n = 0$	Plasma pressure and field strength increase at shock
Oblique shocks	$B_t \neq 0, B_n \neq 0$	

Table 1.2: Possible types of discontinuities in an ideal MHD. Adapted from *Burgess* (1993).

1.2.2 Directional discontinuities

Let us consider discontinuities for which there is a zero mass flux across the surface ($G_n = 0$). This means that the fluid moves parallel to the surface of discontinuity. If $B_n \neq 0$, the velocity, pressure, and magnetic filed must be continuous. The density (and therefore the entropy, temperature, etc.) may have any discontinuity. Such a surface is called a contact discontinuity (CD), and it is simply the boundary between two media at rest relative to the discontinuity which have different densities and temperatures.

On the other hand, if both G_n and B_n are zero, the discontinuity is called tangential (TD). At such a discontinuity, the velocity and the magnetic field are tangential and can have any discontinuity in both magnitude and direction:

$$G_n = 0, \quad B_n = 0, \quad \Delta[V_t] \neq 0, \quad \Delta[B_t] \neq 0. \tag{1.13}$$

The density discontinuity also can take any value, but the pressure discontinuity is related to that of B_t:

$$\Delta[\rho] \neq 0, \quad \Delta\left[P + \frac{B_t^2}{2\mu_0}\right] = 0. \tag{1.14}$$

The discontinuities of the other thermodynamic quantities (entropy, temperature, etc.) are related to those of ρ and P by the equation of state.

Another type of discontinuity, called rotational (RD), is one in which the gas density is continuous. Since the mass flux is continuous, the normal velocity component is continuous also:

$$G_n \neq 0, \quad \Delta[\rho] = 0, \quad \Delta[V_n] = 0. \tag{1.15}$$

For such discontinuity, the energy flux is also continuous ($\Delta[\varepsilon]$=0). Every other thermodynamic quantity is determined if ε and ρ are given. Hence all other thermodynamic quantities including the pressure are continuous. It also follows that B_t is continuous, i.e.,

$$[P] = 0, \quad [B_t] = 0. \tag{1.16}$$

The fact that B_t and B_n are both continuous means that the magnitude of $\boldsymbol{B}$ itself and its angle to the surface are likewise continuous. The vector $\boldsymbol{B}_t$ and the tangential velocity component are discontinuous but the normal velocity component is continuous and its value is

$$V_n = \frac{B_n}{\sqrt{\mu_0 \rho}}. \tag{1.17}$$

1.2.3 Shock waves

Now, we will discuss the type of discontinuity in which

$$G_n \neq 0, \quad \Delta[\rho] \neq 0. \tag{1.18}$$

Such discontinuities are called shock waves. They are characterized by a discontinuity of density and by a fact that the fluid moves through them. The normal component of the magnetic field may or may not be zero.

For shock waves, the vectors $\boldsymbol{B}_{t1}$ and $\boldsymbol{B}_{t2}$ are collinear (indexes 1 and 2 refer to both sides of a shock), i.e., the vectors $\boldsymbol{B}_1$, $\boldsymbol{B}_2$ and the normal to the surface are coplanar,

unlike what happens in tangential and rotational discontinuities, in which the $\boldsymbol{B}_1\,\boldsymbol{n}$ and $\boldsymbol{B}_2\,\boldsymbol{n}$ planes in general do not coincide. The velocity discontinuity $\boldsymbol{V}_{t1} - \boldsymbol{V}_{t2}$ lies in the same plane as $\boldsymbol{B}_1$ and $\boldsymbol{B}_2$. This property, called the coplanarity, is often used in the observational calculation of shock normals.

Among the other conditions that a discontinuity must satisfy to be a shock are (e.g., *Viñas and Scudder*, 1986): (1) that there is density and total temperature jumps in the same sense across the discontinuity, (2) that there should be a decrease of the normal component of the fluid velocity in the direction the density increases, and (3) that the predicted thermal normal pressure must increase with the density.

The shocks are divided into three categories: the fast, slow, and intermediate (also known as Alfvén) which correspond to three modes of small-amplitude waves in MHD. The intermediate shock is a special case because it is shocklike only under some circumstances. In an isotropic plasma, it is not a shock but a rotational discontinuity; there is flow through the boundary but there is no compression of the plasma or dissipation.

The fast and slow shocks have the same behavior in terms of plasma pressure and magnetic field strength as do the corresponding MHD linear waves but the shock-jump conditions are fully nonlinear. Such shocks would be expected to retain the characteristics of the original mode of the wave. Across a fast-mode shock, the magnetic field strength increase but the normal component is constant, so that the increase is all in the transverse component. Therefore, at a fast shock, the downstream magnetic field turns away from the shock normal (Figure 1.12). Conversely, at a slow shock, the downstream magnetic field bends toward the shock normal.

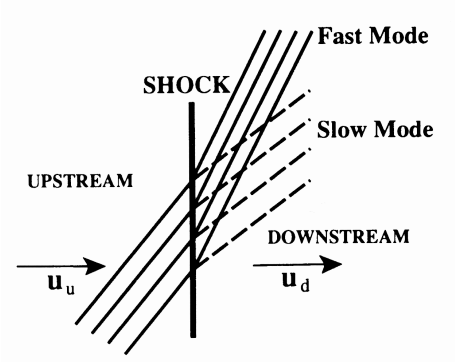

Figure 1.12: Configuration of magnetic-field lines for fast and slow shocks. The field lines are closer together for a fast shock indicating that the field strength increases when the field is bent away from the shock normal. Adapted from *Burgess* (1993).

Figure 1.13 shows changes in the magnetic filed magnitude and plasma parameters (velocity, temperature, and density) as observed by a spacecraft. The fast and slow shocks are further divided into forward and reverse shocks which propagate in the solar wind frame of reference toward the Earth and Sun, respectively. For all shocks, there is a positive change in the velocity magnitude. Changes in all other parameters for a fast forward shock and all, with the exception of magnetic filed magnitude, for a slow forward shock are correlated with the velocity magnitude change. For reversed shocks, these parameters change in opposite sense compared to forward shocks.

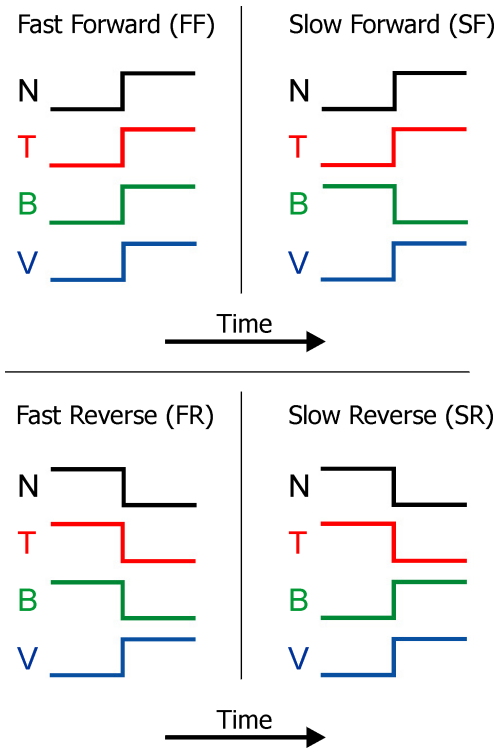

Figure 1.13: Changes of proton speed magnitude (V), temperature (T), density (N), and magnetic field magnitude (B) through fast and slow shocks as observed in the spacecraft frame of reference.

Shocks can also be divided depending on the θ_{Bn} angle (θ_{Bn} is the angle between the shock normal and the orientation of the magnetic field) into parallel (θ_{Bn}=0), perpendicular (θ_{Bn}=90°) and oblique (for θ_{Bn} between 0° and 90°) shocks.

Both parallel and perpendicular shocks have special properties. The parallel shock has the upstream magnetic field parallel to the shock normal ($\boldsymbol{B}_{ut} = 0$). The direction of the magnetic filed remains unchanged across this shock ($\boldsymbol{B}_{dt} = 0$). Because $\boldsymbol{B}_n$ is the only nonzero component of the field and because it does not change, it follows that the total magnetic field is also unchanged by the shock.

At the perpendicular shocks, the upstream magnetic field is perpendicular to the shock normal ($B_{un} = 0$). For such a shock, the upstream and downstream magnetic fields are parallel. The perpendicular shock can only be a fast-mode shock since slow-mode waves do not propagate perpendicular to the magnetic field.

Examples of collisionless shocks are spread throughout the universe. The most widely studied is the Earth's bow shock which is a fast-mode standing shock in the solar wind ahead of the Earth's magnetosphere. In the interplanetary space, there are traveling shocks, called interplanetary (IP) shocks, which separate solar wind flows of different properties. In more exotic astrophysical bodies, one can find jets of material from active galactic nuclei and there probably are shocks formed at the interface between the jet material and the interstellar medium. In supernovas, massive amounts of an energy are deposited in a very short time and shocks are formed as the supernova remnant piles up material as it expands away from the newly formed pulsar.

1.2.4 The Earth's bow shock

A magnetic field of the Earth provides an effective obstacle to the solar wind plasma. Since the solar wind flows super-magnetosonically, the bow shock (BS) is formed in front of the Earth's magnetosphere. The function of this fast non-linear wave is to slow the solar wind to a subsonic speed, so that the solar wind can flow around the magnetosphere. In Figure 1.9, the curve along which the flow and the magnetic field suddenly change from being straight to being curved is the shock front. It has a curved shape close to a paraboloid of revolution. The position of the nose of the bow shock (the most sunward part) is a few R_E ahead of the magnetosphere and at about 14 R_E from the center of the Earth. The exact position of the bow shock is determined by how compressed the flow is on the downstream side of the shock. The plasma that goes through the shock front must pass between the shock and the obstacle so that if it is only weakly compressed, the post shock region will be thick. The factors that control the compression in an ideal fluid are polytropic index γ and the Mach number. If the polytropic index γ is 5/3, the value for an adiabatic process in a monatomic collisional gas, then the solar wind plasma can be compressed by a factor of 4.

Bow shock models

The characteristic shape, position, and motion of the Earth's bow shock have been studied for many years. The bow shock has been modeled using ellipsoidal, paraboloidal, and hyperboloidal surfaces with varying standoff distances under the assumption that its position and shape are determined mainly by the solar wind dynamic pressure, upstream Mach number and direction or magnitude of the interplanetary magnetic field.

Merka et al. (2003) made a comprehensive statistical study of BS models comparing their predictions with BS crossings registered by IMP 8 over 12 years of its observations. During this interval, they found totaly 2293 unambiguous BS crossings for which upstream IMF and solar wind parameters were available. For the study, they chose the Formisano (*Formisano*, 1979) (referred as F79), Němeček and Šafránková (NS91) (*Němeček and Šafránková*, 1991), Farris and Russell (FR94) (*Farris and Russell*, 1994), Cairns and Lyon (CL95) (*Cairns and Lyon*, 1995), and Peredo et al. (P95) (*Peredo et al.*, 1995) models. The basic properties of these models are presented in Table 1.3.

Model	Reference Frame	Symmetry	Parameters
F79	GSE	north-south	P_{sw}
NS91	GSE	north-south	P_{sw}, B, M_{MS}
FR94	SW flow	axial	P_{sw}, B_z, M_{MS}
FR94c	SW flow	axial	P_{sw}, B_z, M_{MS}, R_c
CL95	SW flow	axial	P_{sw}, B_z, M_A, M_S, θ
P95	GIPM	north-south	P_{sw}, B_y, B_z, M_A

Table 1.3: An overview of the basic properties of the bow shock models. Shown parameters are: solar wind dynamic pressure (P_{sw}), IMF magnitude (B) and its components (B_y, B_z), upstream sonic (M_S), Alfvénic (M_A) and magnetosonic (M_{MS}) Mach numbers, radius of curvature of the obstacle (R_c), and the angle between $\boldsymbol{V}_{sw}$ and $\boldsymbol{B}$ (θ). Adapted from *Merka et al.* (2003).

For each observed bow shock crossing, they calculated the bow shock position predicted by each model. Since FR94 and CL95 models predict only a bow shock standoff distance, the authors used approximation of the bow shock shape by paraboloid. The ratio of the predicted to observed bow shock positions R_{mod}/R_{obs} serves as a measure of the prediction accuracy. As an example, bow shock crossings for the whole set of IMF/SW conditions are shown for all models in Figure 1.14.

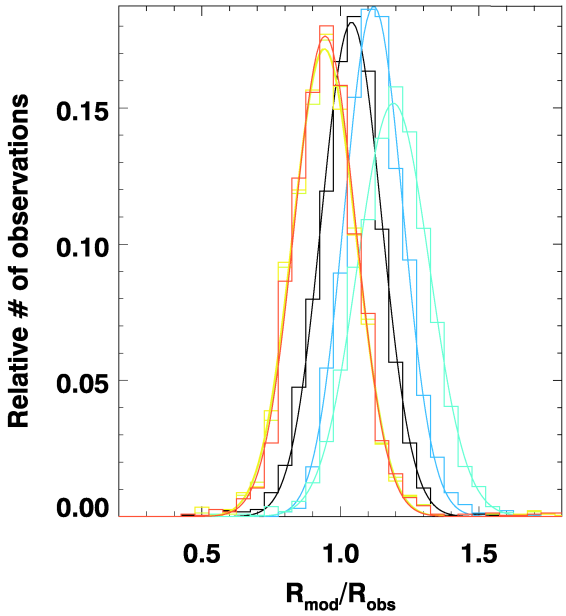

Figure 1.14: The ratio of radius vectors of model predicted and observed bow shock positions are depicted as histograms with Gaussian fits. Used models are distinguished by different colors: P95 — cyan, FR94c — green, FR94 — orange, CL95 — red, F79 — black, and NS91 — blue. Adapted from *Merka et al.* (2003).

The authors investigated these model reliability in a whole range of IMF/SW conditions (including unusual conditions) and concluded that the predictions of F79, FR94, FR94c, CL95 are the most accurate with F79 giving a slightly better result. The widely used P95 model seems to be biased by $\sim$20%, consistently with note in *Šafránková et al.* (1999a,b) and the original paper by *Peredo et al.* (1995). For large values of IMF and its components and for low upstream Mach numbers, all models except NS91 underestimate the BS distance. The same effect was found for changes in the relative orientation of the IMF and solar wind velocity vector (see Figures 4-6 in *Merka et al.* (2003)). According to a discussion to these figures, a simple dependence on the IMF magnitude in NS91 is sufficient to explain the shifts for B_y and B_z.

From Figures 4–6 in *Merka et al.* (2003), it also follows that the NS91 model, in contrast to other models, is nearly independent on the variations of IMF and its components as well as on extreme values of solar wind parameters. *Jeřáb et al.* (2005) used this advantage of the NS91 model and corrected the model in order to exclude overestimation of the BS position.

1.2.5 Interplanetary shocks

There are two sources of interplanetary shocks (Figure 1.15): coronal transients, which can be accounted for almost wholly by coronal mass ejections (*Luhmann*, 1995), and corotating interaction regions (CIRs). Coronal mass ejections (CMEs) are defined as transient changes in the corona that are often observed in coronagraphs as expanding ejected loops of material of enhanced density. On the other hand, the solar wind has low-speed and high-speed streams, coming from different source regions on the Sun. The Sun rotation leads to overtaking of a slow stream by a fast one and formation of a CIR. CMEs and CIRs drive interplanetary shocks if they move at super-magnetosonic velocities with respect to the ambient solar wind.

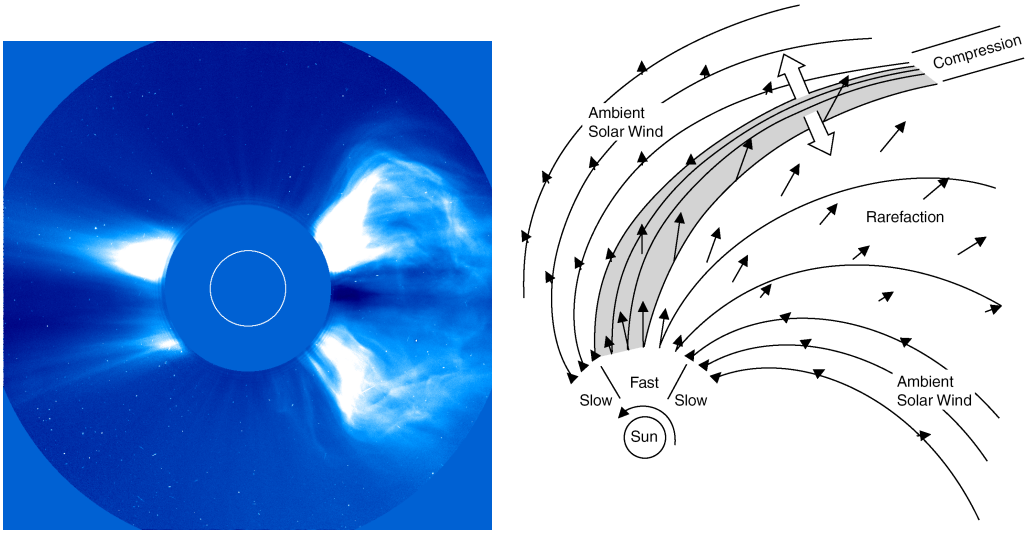

Figure 1.15: Sources of interplanetary shocks: *left* — A coronal mass ejection as recorded by the SOHO LASCO C2 coronagraph on November 6, 1997; *right* — Collision of a fast stream with a slow stream of the solar wind to produce a corotating interaction region (adapted from *Pizzo*, 1985).

Lindsay et al. (1994) analyzed IP shocks observed by Pioneer Venus Orbiter at 0.72 AU during 1979-1988. They found that the primary mechanism driving IP shocks at 0.72 AU is the coronal mass ejection. Interplanetary shocks also result from stream and complex interactions but these causes constitute only 20% of all cases considered. The strength of both CMEs and stream interactions at 0.72 AU varies during the solar cycle. CMEs produce more interplanetary shocks during the maximum phase of the solar cycle so, therefore, must have velocities higher during this period than at solar minimum. More stream interactions produce interplanetary shocks at 0.72 AU during the declining phase of the solar cycle, suggesting that the highest velocity streams are seen during the declining phase of the solar cycle.

In order to understand shock source contributions as a function of radial distance and heliolatitude, *Luhmann* (1995) analyzed earlier studies based on observations of Helios, Pioneer, Voyager, and Ulysses. The author shows that interplanetary shocks are generally inner-to-middle heliosphere features of the solar wind. The transient source dominates the inner heliosphere at radial distances ≤ 2 AU, while stream interactions probably compete

IP shock parameters	All shocks	Forward shocks	Reverse shocks	CIR driven (forward)	T. driven (forward)	Unknown driver
V, km/s	90±40	78±28	145±42	72±23	91±26	78±28
V_x GSE, km/s	-426±81	-397±63	-524±56	-382±42	-412±84	-380±43
V_y GSE, km/s	-2±42	-16±30	35±43	-24±27	-6±31	2±30
V_z GSE, km/s	0±48	5±37	7±71	13±31	8±71	14±48
M_s	1.44±0.35	1.39±0.34	1.66±0.345	1.31±0.26	1.66±0.40	1.125±0.08
$\phi_{\mathbf{n}}$ GSE, deg	————	185±23	9±31	193±23	175±21	180±30
$\theta_{\mathbf{n}}$ GSE, deg	8±32	13±30	0±37	22±30	2±29	40±15
θ_{Bn}, deg	59±24	62±21	60±22	57±22	54±28	72±15

Table 1.4: Parameters of IP shocks depending on shock type (forward and reverse) and driver (CIR — corotating interaction region and T. — transient) observed by Wind during its first 2.5 years of operation. Shown are: shock speed relative to the upstream solar wind velocity (V), components of the shock velocity in GSE coordinates (V_x, V_y, V_z), magnetosonic Mach number (M_s), GSE azimuth (ϕ_n) and latitude (θ_n) of shock normal direction, and the angle between shock normal and upstream magnetic field (θ_{Bn}). Adapted from *Berdichevsky et al.* (2000).

with or dominate this source between 3 and 10 AU. Only few shocks were found beyond $\sim$20 AU. Both sources contribute to a shock activity at moderate to high heliolatitudes with interesting difference from their lower latitude counterparts related to 3-D properties of a stream structure and higher speed of the ambient solar wind.

More recently, *Berdichevsky et al.* (2000) made a comprehensive analysis of interplanetary shocks observed by Wind during its first 2.5 year of operation (from November 1994 to May 1997). This period corresponds to the decreasing phase of 22nd and start of the 23rd solar cycle. The authors determined shock drivers and accurately calculated shock parameters which include: shock velocity ($\boldsymbol{V}$), magnetosonic Mach number (M_s), azimuth (ϕ_n) and latitude (θ_n) of shock normal direction, and the shock obliquity (θ_{Bn}) relative to the upstream magnetic field. A summary of shock parameters according to the shock drivers are presented in Table 1.4. The authors also found that the mean strength and a rate of occurrence of the shocks correlate with the solar cycle and that both show a decrease in 1996, consistent with the time of the lowest ultraviolet solar radiance indicative of the solar minimum. A higher frequency of occurrence and a larger variety in shock strengths were observed before and after 1996.

A comparison of shock properties for solar minimum and solar maximum was made by *Echer et al.* (2003). They analyzed data from Wind for the 1995-1996 solar minimum and from ACE for the 2000 solar maximum and found 25 and 57 shocks, respectively. Figure 1.16 shows bar graph expressing a percentage of different shock types. As seen from the figure, the majority of shocks is of the fast forward type, 88% for the solar maximum and 60% for the solar minimum.

The distributions of interplanetary shock parameters (Figure 1.17) show that the average shock speed is significantly higher for the solar maximum compared to the solar minimum. The average values of Alfvén Mach numbers are very similar for the solar minimum and solar maximum, however, their distributions are completely different. On the other hand, both compression ratios have similar averages and distributions for the

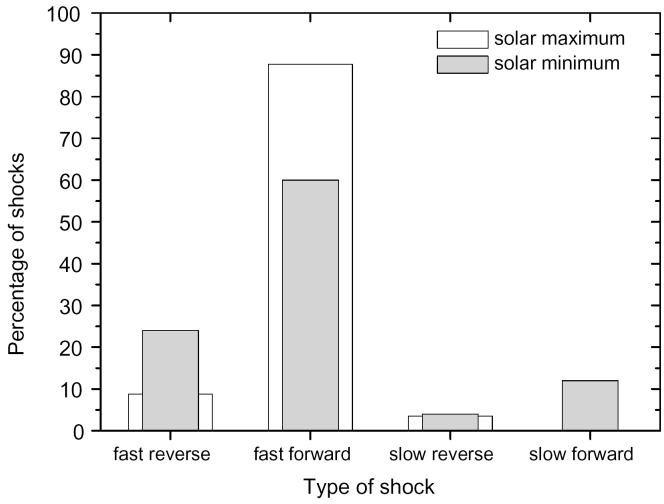

Figure 1.16: Percentage of interplanetary shock types for the solar maximum (white bars) and solar minimum (gray bars). Adapted from *Echer et al.* (2003).

solar minimum and solar maximum.

1.2.6 Relationship of interplanetary shocks to geomagnetic disturbances

The main reason why to study the IP shocks and other solar wind discontinuities is their relationship to geomagnetic disturbances. It was first pointed out by *Tsurutani et al.* (1995) and later studied by other authors (e.g., *Gonzalez et al.*, 1999; *Tsurutani and Gonzalez*, 1998) but many aspects of this problem are still under debate because the interaction of the solar wind with the magnetosphere is a very complex process.

The magnetic field at the Earth surface is a sum of an internal dipole magnetic field and magnetic fields of currents flowing in the magnetosphere and along its boundary. The current carriers are solar wind particles penetrating into the magnetosphere by a variety of processes. The penetrating particles are partly trapped and stored in the geomagnetic field and from time to time released explosively into an interplanetary space. Such process is called geomagnetic storm or substorm. The magnetospheric currents are intensified during substorms and their contribution to the magnetospheric magnetic field increases. The deviation of the magnetic field measured on the Earth surface can be as high as 1500 nT and can last for several hours. A weighted mean deviation measured at several points on the Earth surface is called the Dst index and it is used as a measure of the geomagnetic disturbance strength.

Among solar wind disturbances, IP shocks have been identified as sources of largest geomagnetic storms. As noticed in Section 1.2.5, the two principal mechanisms driving IP shocks are corotating interaction regions (CIRs) and coronal mass ejections (CMEs). CIRs are characterized by a fluctuating magnetic field and they produce only weak or moderate storms (*Tsurutani et al.*, 1995). Intense magnetic storms tend to develop when a southward-pointing IMF (B_z <-10 nT) lasts more than three hours (*Gonzalez and Tsurutani*, 1987) and such storms are often associated with CMEs.

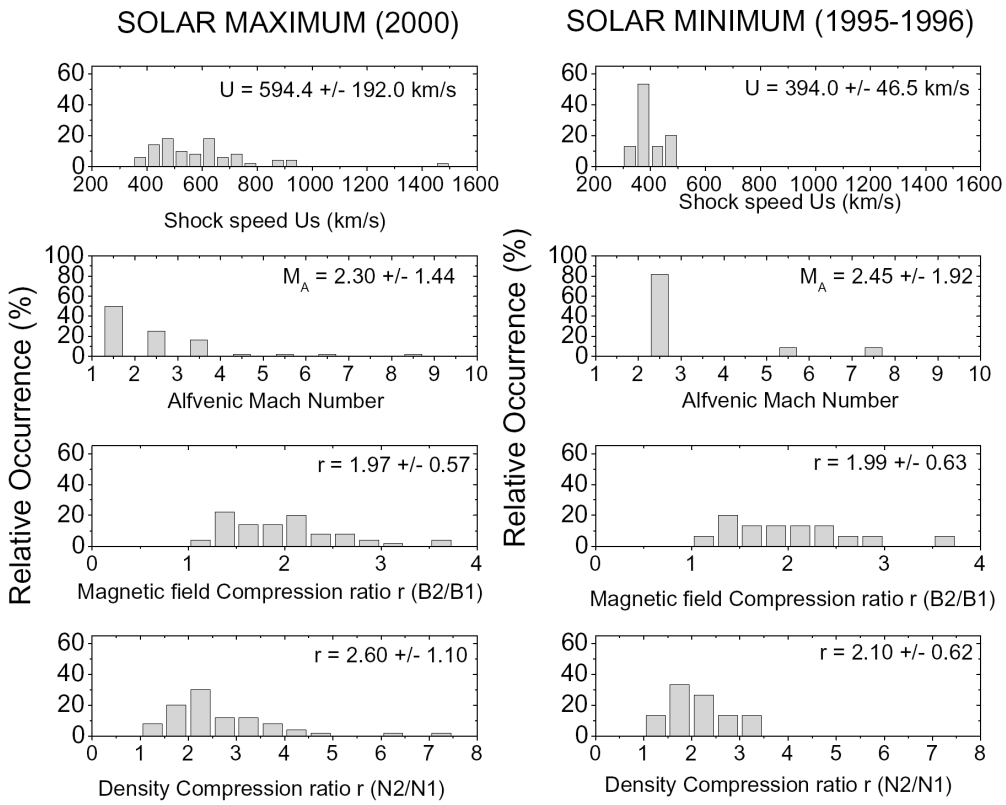

Figure 1.17: Distributions of IP shock parameters for the solar maximum (*left*) and solar minimum (*right*). Shown are: shock speed (U_s), Alfvén Mach number (M_A), magnetic (B_2/B_1) and density (N_2/N_1) compression ratios. Adapted from *Echer et al.* (2003).

In order to examine the influence of shock parameters on geomagnetic disturbances following the shock arrival at the Earth, *Jurac et al.* (2002) analyzed 107 fast, forward-propagating interplanetary shocks observed by Wind from 1995 to 2000. They found that the angle between the shock front normal and the IMF direction might play a useful role in forecasting the severity of geomagnetic storms occurring within 48 hours after the shock passage. Quasi-perpendicular shocks, i.e., those nearly orthogonal to the IMF direction, constrain IMF components in the plane parallel to the shock front, making it more likely to produce southward IMF. The authors demonstrated that, regardless of the shock driver, about 40% of forward IP shocks result in intense magnetic storms (Dst < -100) when the shock normal is almost perpendicular to the upstream IMF (θ_{Bn} between 70° and 90°), compared to about 10–15% of shocks with normals not perpendicular to the IMF direction (Figure 1.18).

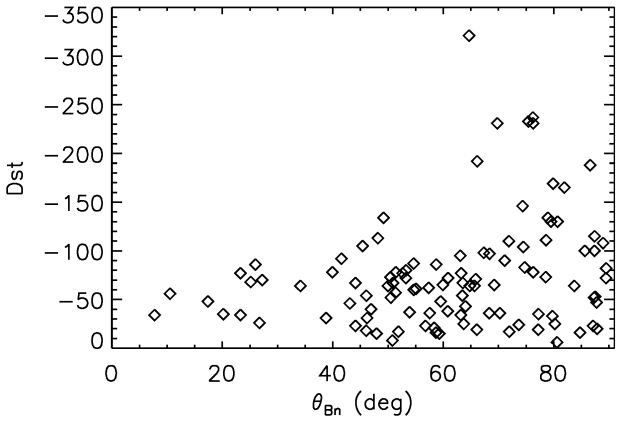

Figure 1.18: Shock geoeffectiveness as a function of the angle between shock normal and upstream IMF (θ_{Bn}). Adapted from *Jurac et al.* (2002).

1.3 Methods for discontinuity and shock parameter determination

The discontinuity and shock characteristics (normal direction, propagation speed, and values of upstream and downstream plasma and magnetic field parameters which best describe the discontinuity) can be determined by different methods, either from observations at a single spacecraft using the magnetic field, possibly accompanied with solar wind data, or from simultaneous multiple spacecraft measurements.

1.3.1 Single-spacecraft methods

The single-spacecraft methods use different subsets of the full set of conservation lows (1.7) — (1.12). They can be divided into several groups. Variance analysis is based on a search for a coordinate system in which one component of the magnetic (electric) filed exhibits minimum (maximum) change. The method can be applied for both directional discontinuity and shock analysis. Coplanarity methods, which is applicable only for shock

analysis, make use of the fact that upstream and downstream magnetic fields and the velocity discontinuity should lie in the same plane as the shock normal. These methods can provide only the normal direction and thus the velocity of a shock is usually computed from the mass flux conservation low (1.7):

$$V_s = \frac{\Delta[\rho \boldsymbol{V}]}{\Delta[\rho]} \cdot \boldsymbol{n} \tag{1.19}$$

The variance analysis and coplanarity methods are straight-forward and provide a unique solution for shock parameters. More sophisticated methods use larger sets of jump conditions and an iterative procedure.

Variance analysis

The main purpose of minimum or maximum variance analysis (MVA) is to find, from single spacecraft data, an estimator for the direction normal to a discontinuity surface. Unlike all other methods described below, the variance methods deal with variations within the transition rather than the observations taken well upstream and downstream of the transition.

A single spacecraft passing through the discontinuity surface observes variations in the magnetic field. Since $\nabla \boldsymbol{B} = 0$, the normal component of the magnetic field must remain constant. It follows that if a unique direction can be found such that the variation in the magnetic field along that direction is zero (or at least minimized to a sufficient extent), then this direction corresponds to the normal direction. When considering the electric field, an opposite argument holds: the tangential component of $\boldsymbol{E}$ should be continuous through such a layer, so the normal direction will correspond to that of maximum variance in $\boldsymbol{E}$.

Coplanarity

The normal to a planar surface can be determined if two vectors which lie within the surface can be found. As was noticed in Section 1.2.3, for a shock surface these vectors include the change in the magnetic field, the cross-product of the upstream and downstream magnetic fields, and the cross-product between the upstream or downstream magnetic fields or their difference with the change in bulk flow velocity. These vectors give rise to constraint equations for the shock normal:

$$\Delta[\boldsymbol{B}] \cdot \boldsymbol{n} = 0 \tag{1.20}$$

$$(\boldsymbol{B}_d \times \boldsymbol{B}_u) \cdot \boldsymbol{n} = 0 \tag{1.21}$$

$$(\boldsymbol{B}_u \times \Delta[\boldsymbol{V}]) \cdot \boldsymbol{n} = 0 \tag{1.22}$$

$$(\boldsymbol{B}_d \times \Delta[\boldsymbol{V}]) \cdot \boldsymbol{n} = 0 \tag{1.23}$$

$$(\Delta[\boldsymbol{B}] \times \Delta[\boldsymbol{V}]) \cdot \boldsymbol{n} = 0 \tag{1.24}$$

where the velocity jump $\Delta[\boldsymbol{V}]$ can be measured in any frame (e.g., in the spacecraft frame of reference).

Any pair of vectors which are dotted with $\boldsymbol{n}$ in the above constraints can be used to find the shock normal. The resulted methods are known as magnetic coplanarity (*Lepping and Argentiero*, 1971) and the mixed data methods of Abraham-Shrauner (*Abraham-Shrauner and Yun*, 1976):

$$\boldsymbol{n}_{MC} = \pm\frac{(\boldsymbol{B}_d \times \boldsymbol{B}_u) \times \Delta[\boldsymbol{B}]}{|(\boldsymbol{B}_d \times \boldsymbol{B}_u) \times \Delta[\boldsymbol{B}]|} \tag{1.25}$$

$$\boldsymbol{n}_{MX1} = \pm\frac{(\boldsymbol{B}_u \times \Delta[\boldsymbol{V}]) \times \Delta[\boldsymbol{B}]}{|(\boldsymbol{B}_u \times \Delta[\boldsymbol{V}]) \times \Delta[\boldsymbol{B}]|} \tag{1.26}$$

$$\boldsymbol{n}_{MX2} = \pm\frac{(\boldsymbol{B}_d \times \Delta[\boldsymbol{V}]) \times \Delta[\boldsymbol{B}]}{|(\boldsymbol{B}_d \times \Delta[\boldsymbol{V}]) \times \Delta[\boldsymbol{B}]|} \tag{1.27}$$

$$\boldsymbol{n}_{MX3} = \pm\frac{(\Delta[\boldsymbol{B}] \times \Delta[\boldsymbol{V}]) \times \Delta[\boldsymbol{B}]}{|(\Delta[\boldsymbol{B}] \times \Delta[\boldsymbol{V}]) \times \Delta[\boldsymbol{B}]|} \tag{1.28}$$

The magnetic coplanarity is easy to apply since it requires only magnetic field data, but it fails for θ_{Bn}=0° or 90°.

There is also an approximate normal, the velocity coplanarity normal (*Abraham-Shrauner*, 1972), given by

$$\boldsymbol{n}_{VC} = \pm\frac{\boldsymbol{V}_d - \boldsymbol{V}_u}{|\boldsymbol{V}_d - \boldsymbol{V}_u|} \tag{1.29}$$

which is an approximation valid at high Mach numbers and for θ_{Bn} near 0° and 90°.

Shock jump conditions

Each of the previous methods uses a small subset of the Rankine-Hugoniot conservation equations to determine the shock normal and speed. A potentially more reliable approach is to take into account more of the Rankine-Hugoniot conservation equations in order to establish a full set of upstream and downstream quantities (including the shock normal direction) which best satisfy these physical laws.

Lepping and Argentiero (1971) first put such a scheme together. The method solves a slightly expanded subset of Rankine-Hugoniot conservation equations for the asymptotic magnetofluid variables. These equations are subsequently augmented with the magnetic coplanarity and mass flux conservation equations to determine the shock normal direction and the shock speed. The method is self-consistent, however, it has to find the solution in an 11-dimensional parameter space which raises the question of uniqueness of the solution.

Later, *Viñas and Scudder* (1986) overcame this difficulty. They developed a fast iterative method for the determination of geometrical characteristics of a shock, conservation constants and self-consistent asymptotic magnetofluid variables based on a six-equation subset of RH conservation equations. The subset is chosen to avoid using those equations that explicitly involve the temperature. The method provides explicit proofs of "uniqueness" (or lack thereof) of the solutions and, in addition, converges quickly for either quasi-parallel or quasi-perpendicular shocks.

Szabo (1994) improved the *Viñas and Scudder* (1986) method by including the plasma temperature observations through the perpendicular momentum flux and energy density flux conservation equations that allowed him to remove spurious solutions given by the

Viñas and Scudder (1986) method without a manual intervention. This method also develops proper error propagation from observational uncertainties establishing uncertainty regions for computed shock normal directions and speeds.

1.3.2 Multi-spacecraft methods

It often happens that there are more than one spacecraft simultaneously monitoring solar wind parameters. Thus, a discontinuity propagating in the solar wind is observed by these spacecraft and information of the spacecraft positions and times of the discontinuity passages can be used to construct the surface normal direction and propagation velocity (e.g., *Russell et al.*, 1983), since

$$\boldsymbol{r}_{\alpha\beta} \cdot \boldsymbol{n} = V_d \cdot t_{\alpha\beta} \tag{1.30}$$

where $\boldsymbol{r}_{\alpha\beta}$ is the separation vector between α and β spacecraft and $t_{\alpha\beta}$ is the time difference between observations of a particular boundary. Given four spacecraft, the normal vector $\boldsymbol{n}$ and propagation velocity V_d can be found from the solution of the following system:

$$\begin{pmatrix} \boldsymbol{r_{12}} \\ \boldsymbol{r_{13}} \\ \boldsymbol{r_{14}} \end{pmatrix} \begin{pmatrix} \boldsymbol{n_x} \\ \boldsymbol{n_y} \\ \boldsymbol{n_z} \end{pmatrix} \cdot \frac{1}{V_d} = \begin{pmatrix} \boldsymbol{t_{12}} \\ \boldsymbol{t_{13}} \\ \boldsymbol{t_{14}} \end{pmatrix} \tag{1.31}$$

For a shock surface, it is also possible to use any of the equations (1.20) – (1.24). Thus, depending on the number of spacecraft that observe a shock passage, the shock parameters can be uniquely determined either solely from the spacecraft positions and times of passages or together with magnetic field and plasma parameters measured by an individual spacecraft. For example, the system

$$\begin{pmatrix} \boldsymbol{r_{12}} \\ \boldsymbol{r_{13}} \\ \Delta[\boldsymbol{B}] \end{pmatrix} \begin{pmatrix} \boldsymbol{n_x} \\ \boldsymbol{n_y} \\ \boldsymbol{n_z} \end{pmatrix} \cdot \frac{1}{V_d} = \begin{pmatrix} \boldsymbol{t_{12}} \\ \boldsymbol{t_{13}} \\ 0 \end{pmatrix} \tag{1.32}$$

makes use of equation (1.20).

However, in order to increase the accuracy of shock parameter determination, it is possible to take into account more of the equations (1.20) – (1.24). In this case, the system will contain more equations than unknowns that precludes from determination of a unique solution. Thus, weighting of the equations based on uncertainties in the spacecraft positions, times of passages, magnetic field and plasma measurements should be used for determination of the most probable shock parameters.

1.3.3 Difficulties of discontinuity and shock parameter determinations

In this section, we would like to mention the problems connected with normal computations and their usage and to discuss an accuracy of different computation techniques.

Rotational vs. tangential discontinuities

An accurate determination of a directional discontinuity orientation is essential for categorization it into RD or TD. In the MHD theory, the field component $|B_n|$ normal to the discontinuity surface vanishes for TD, whereas it is arbitrary for RD.

Directional discontinuities are often classified using the *Smith* (1973) method which is based on two parameters: the field normal component $|B_n|$ and the change of field magnitude $|\Delta[B]|$ across the transition. Both parameters are normalized by the maximum magnitude B_{max} upstream and downstream of the discontinuity. Following *Smith* (1973), *Neugebauer et al.* (1984) identified four classes of events:

Rotational (RD):	$\|B_n\|/B_{max} \geq 0.4$	$\|\Delta[B]\|/B_{max} < 0.2$
Tangential (TD):	$\|B_n\|/B_{max} < 0.4$	$\|\Delta[B]\|/B_{max} \geq 0.2$
Either (ED):	$\|B_n\|/B_{max} < 0.4$	$\|\Delta[B]\|/B_{max} < 0.2$
Neither (ND):	$\|B_n\|/B_{max} \geq 0.4$	$\|\Delta[B]\|/B_{max} \geq 0.2$

A value of 0.4 for the $|B_n|/B_{max}$ was arbitrarily chosen as a likely value when minimum variance analysis normal estimates are used, while a value of 0.2 for the $|\Delta[B]|/B_{max}$ is reasoned by error estimate arguments and the assumption of an isotropic solar wind.

The following percentages for RD:TD:ED:ND have been found using this classification method: *Smith* (1973): 37:15:47:1, *Lepping and Benhannon* (1980): 38:18:38:6, *Neugebauer et al.* (1984): 56:12:32:1. It should be noted that in these studies only single-spacecraft magnetic field data were used and the MVA was applied for the determination of discontinuity normal direction.

Recently, *Horbury et al.* (2001) analyzed discontinuities which were simultaneously observed by Geotail, Wind and IMP 8 located in the solar wind. Using the bulk velocity measured by Geotail and assuming that a discontinuity is stationary in the plasma frame, they calculated orientations of discontinuity surfaces from the spacecraft positions and times of discontinuity observations. They found the following percentage for RD:TD:ED:ND: 9:14:74:3, with a much lower fraction of clear RDs and many more EDs compared to the same set of discontinuities when MVA is applies to the Wind magnetic field data (57:11:26:6).

Finally, *Knetter et al.* (2004) accomplished a detailed statistical analysis of interplanetary discontinuities using magnetic field data from the four Cluster spacecraft. In order to find the surface normals, they used MVA and four-spacecraft timing methods. Figure 1.19 shows a scatter-plot based on normal estimates by both methods.

The resulting percentages using MVA (35:16:47:2) are consistent with earlier studies. However, the timing derived normals yield different results. Almost all DDs (99%) appear to have a magnetic field normal component $|B_n|/B_{max}$ <0.4 in contrast to only 63% when MVA normal estimates are used. The four spacecraft timing percentage (0:16:83:1) shows that there is no unambiguous RDs and only 16% can be identified as clearly tangential. The majority of the discontinuities (83%) can be either rotational or tangential. Varying the parameter controlling the MVA accuracy, the authors show that the observed discrepancies between the two methods are caused by inaccuracies of MVA estimates.

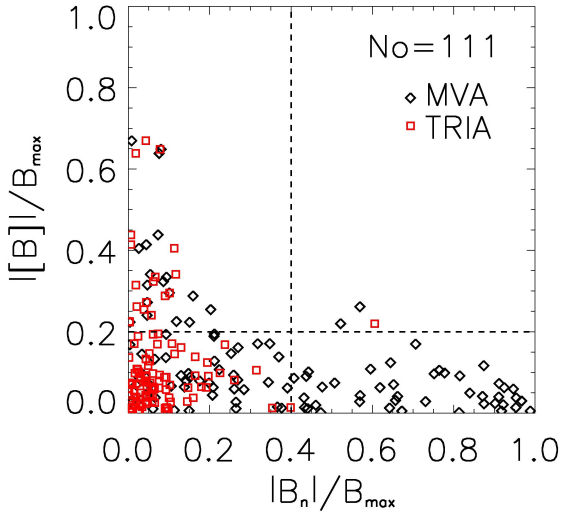

Figure 1.19: Scatter-plot based on normal estimates from four spacecraft timing (red squares) and Cluster 4 MVA (black diamonds). Adapted from *Knetter et al.* (2003).

Influence of multi-ion population and thermal anisotropy on shock parameter determination

Kessel et al. (1994) adapted the single-ion *Viñas and Scudder* (1986) solution of the RH problem to a multiple-ion solution. They analyzed quasi-perpendicular inbound and quasi-parallel outbound crossings at comet Halley. The results show that in both cases, there are differences between the single- and multi-ion solutions with the multi-ion solutions being the more reliable. They also examined parameter regimes in which a multi-ion solution is relevant. The largest difference was found to occur for quasi-parallel shocks, small values of solar wind speed, large values of heavy ion density, and very strong and very weak shocks.

Some estimates of the influence of proton thermal anisotropy have also been made. For example, *Neubauer* (1970) analyzed the jump relations for shocks moving into collision-free anisotropic magnetized plasma under the assumption of plasma isotropy behind the shock front. He showed that the influence of the anisotropy is greatest for nearly equal thermal and magnetic energy densities.

Lepping (1972) explored the influence of thermal anisotropy on least-squares estimates of interplanetary shock parameters and the associated normals by using the RH equations. Although the method is restricted to six equations that do not explicitly involve thermal pressure (or temperature), it allows for nonunity anisotropy factors. The author applied this method and analyzed a fast shock observed by Explorer 33 and 35. However, he found only a weak relationship between the thermal anisotropy and shock parameters in this particular case.

Accuracy of methods for shock parameter determination

A comprehensive analysis of accuracy of methods for shock parameter determination has been made by *Berdichevsky et al.* (2000). They analyzed interplanetary shocks observed by Wind over its first 2.5 years of observations and accurately computed shock parameters

by two methods: 1) a combination of the "preaveraged" magnetic-coplanarity, velocity coplanarity, and the Abraham-Shrauner-mixed methods, and 2) the *Viñas and Scudder* (1986) method. They found that the traditional "parameter averaging methods" could be used with a high degree of confidence in most cases if the right time intervals upstream and downstream of the IP shock are chosen.

Also *Russell et al.* (2000) compared several different methods of shock normal determinations and speed estimations and concluded that of the single-spacecraft methods, magnetic coplanarity is most accurate and the mixed-mode techniques were next most accurate.

Using four spacecraft to observe solar wind magnetic discontinuities, *Knetter et al.* (2003) estimated their orientations by relative timing referred to as triangulation. Besides triangulation, they applied MVA and they conclude that MVA results are often far from the triangulation normals and there are often great discrepancies between four MVA normals among each other. They believe that the MVA normal estimates are generally influenced by the presence of non-isotropic magnetic fluctuation due to 3-D wave fields.

1.4 Interaction of discontinuities with the bow shock

Interactions of solar wind discontinuities with the Earth's bow shock lead to phenomena that have a significant influence on the Earth's magnetosphere. One of the most interesting of them are hot flow anomalies (HFAs) which are the results of the IMF tangential discontinuity interactions with the bow shock and IP shocks which propagate into the magnetosheath and have a direct impact on the Earth's magnetosphere.

1.4.1 Hot flow anomalies

Regions of hot, highly deflected plasma often containing depressed magnetic field near the Earth's bow shock were discovered in the 1980s (*Schwartz et al.*, 1985; *Thomsen et al.*, 1986). The main observational features of HFAs include (*Schwartz*, 1995): (1) edge regions of enhanced magnetic field strength, density, and a slight increase in temperature. The outer edges of these enhancements are fast shocks generated by pressure enhancements within the core region. The inner edges of the enhancements are probably tangential discontinuities (*Paschmann et al.*, 1988). (2) The central regions of HFAs contain hot (10^6–10^7 K) plasma flowing significantly slower than the ambient solar wind in a direction highly deflected, in many cases nearly 90° from the Sun-Earth line. The flow velocity is often roughly tangential to the nominal bow shock shape (*Schwartz et al.*, 1988). (3) HFAs are associated with large changes in the IMF direction. Typically, the angle between the pre- and post-event fields is $\sim$70°.

It has been suggested that a formation of these events is due to the interaction of the bow shock with tangential or rotational discontinuities (*Schwartz et al.*, 1988; *Paschmann et al.*, 1988; *Thomas et al.*, 1991; *Thomsen et al.*, 1988). Kinetic simulations confirm that the interaction of IMF discontinuities with the bow shock can produce events with HFA characteristics (*Thomas et al.*, 1991; *Lin*, 1997). Using a test particle calculation associated with the interaction between the bow shock and TD, *Burgess* (1989) has shown that anomalous flows can be formed by specularly reflected ions moving upstream of the

bow shock along a certain type of TD, where a motional electric field associated with the upstream bulk flow focuses reflected ions towards TD from either side of the TD.

Schwartz et al. (2000) investigating set of 30 HFAs have defined conditions for the HFA formation: (1) an interplanetary current sheet with a motional electric field which points towards it on at least one side; (2) current sheets whose normals make a large cone angle with the sunward direction; (3) tangential discontinuities (probably). Suggesting that all TDs above 60° of the cone angle with towards electric field on at least one side result in HFAs, the authors have estimated an occurrence rate of $\sim$3 HFAs per day which is entirely consistent with observations.

Such HFA features should be swept downstream, however, only a few HFAs have been observed in the magnetosheath (*Paschmann et al.*, 1988; *Thomsen et al.*, 1988; *Schwartz et al.*, 1988; *Šafránková et al.*, 2000). Although almost all reported magnetosheath events have been identified near the bow shock, they may influence significantly the magnetosphere. *Sibeck et al.* (1999) have demonstrated a remarkable magnetospheric response to an IMF tangential discontinuity which resulted in a sunward magnetopause displacement exceeding 5 R_E. The authors show that the underlying IMF TD was not unaccompanied by any significant plasma variation and was itself totally unremarkable, and conclude that such transient but dramatic disturbances of the magnetosphere are common.

Recent study of *Šafránková et al.* (2000) suggests a negligible evolution of HFAs in the magnetosheath. The authors have pointed out that HFAs must be rather frequent in the central magnetosheath and little evidence for them in the literature may be attributed to the difficulties of distinguishing them among other phenomena in a highly disturbed magnetosheath flow. The magnetosheath HFAs exhibit a clear tendency to occur predominantly during periods of enhanced solar wind speed. A similar tendency can be inferred from the list of HFAs observed by ISEE and AMPTE (*Onsager et al.*, 1990). *Šafránková et al.* (2000) have also shown a double structure of some magnetosheath HFAs which is probably connected with the mechanism of the HFA formation in front of the bow shock. Magnetosheath double HFAs are distinguished by the ion flux enhancement that divides a core region into two parts. Consecutive study (*Šafránková et al.*, 2002) has pointed out that plasma parameters inside this enhancement are similar to those in the surrounding undisturbed magnetosheath. The principal rotation of the magnetic field from pre-event to post-event orientations occurs inside the HFA core and not on its boundaries. This field rotation usually, but not always, coincides with the center of the aforementioned flux enhancement. High-energy (tens of keV) electrons are present in one of these parts. Similar double structure of HFAs was observed in the solar wind as well (*Vaisberg et al.*, 1999). It is probably consistent with a slight density enhancement at the center of the HFA core region seen in *Lin* (1997) two-dimensional hybrid simulations.

HFAs should be distinguished from more frequent foreshock cavities (*Sibeck et al.*, 2002). Foreshock cavities resemble some characteristics of HFAs like a duration of several minutes, reduced densities and magnetic field strengths flanked by enhancements, and enhanced ion temperatures that increase gradually from the solar wind towards the core regions of events. However, many characteristics of the foreshock cavities differ from those of HFAs. There is no great reduction or deflection of ion flow velocities within the evens, the ion populations never become nearly isotropic, ion temperatures never reach the value previously reported for HFAs, and pressures within the cavities are only slightly greater than those outside. Moreover, none of the previously observed foreshock cavities

are accompanied with IMF discontinuities.

1.4.2 Interplanetary shocks in the magnetosheath

Before analyzing propagation of IP shocks in the magnetosheath, the shock parameters in the solar wind should be determined. IP shocks in the solar wind are generally assumed to be planar on the scale size of the Earth's magnetosphere (e.g., *Russell et al.*, 2000). *Russell et al.* (2000) analyzed a single IP shock with four solar wind spacecraft and found that normals calculated from the data of three of them were consistent with the planarity assumption (with the accuracy of the travel time estimates).

However, a deviation from the planarity has been also reported (e.g., *Russell et al.*, 1983; *Šafránková et al.*, 1998; *Szabo et al.*, 2001; *Szabo*, 2005). For example, *Szabo et al.* (2001) analyzed six magnetic cloud driven IP shocks, each observed by two spacecraft located in the solar wind (either Wind and ACE or Wind and IMP 8). The calculated local shock front orientations indicate that IP shocks driven by slow and small magnetic clouds have a significant level of corrugation, mostly limited to the plane perpendicular to the cloud axis. On the other hand, fast and large magnetic clouds, if they are encountered close to the center, drive nearly planar shocks.

Recently, *Szabo* (2005) analyzed an IP shock observed by five spacecraft in the solar wind. Using the magnetic field and plasma data measured by three spacecraft (Wind, ACE, and IMP 8) and applying the complete set of the Rankine-Hugoniot conservation equations, the author calculated local shock normals at the positions of these spacecraft. These local normals were then compared with five global shock orientations calculated from four-spacecraft positions and times of the shock passages. Analyzing the differences in the shock normal orientations, *Szabo* (2005) concluded that there exist small scale (few R_E) ripples or corrugation on the surface of the shock.

The interaction of IP shocks with the bow shock and their transmission through the magnetosheath have been studied by gasdynamic (e.g., *Dryer*, 1973; *Spreiter and Stahara*, 1992) and MHD (e.g., *Whang*, 1991; *Yan and Lee*, 1996) modeling. The gasdynamic models allow the generation and propagation of only fast forward shocks in the magnetosheath, thus they find only a single, fast mode pressure pulse (or a fast shock in the supersonic flanks) propagating through the magnetosheath. On the other hand, MHD models predict a more complicated scenario. For example, the one-dimensional MHD modeling of *Yan and Lee* (1996) suggests that, if an incident forward shock transmits through the bow shock, a fast shock, a slow expansion wave, a slow shock, and a contact discontinuity are generated downstream of the bow shock. If the incident shock is a reverse shock, the generated fast shock becomes a fast expansion wave.

Parameters of a shock propagating through the magnetosheath are essential for prediction of the shock arrival to the magnetosphere. As an example, Figure 1.20 displays results of the *Spreiter and Stahara* (1992) modeling. The presented snapshot views show plasma pressure contours at four sequential times as a planar interplanetary shock passes a terrestrial magnetopause obstacle. The results show that the trace of the interplanetary shock in the magnetosheath remains nearly planar as it moves through the magnetosheath and that the extent of the transition flow region is relatively short. This prediction is supported by observations reported by *Szabo et al.* (2000). Moreover, *Szabo* (2004) analyzed IP shock surface normals and propagation speeds in the solar wind and estimated the pre-

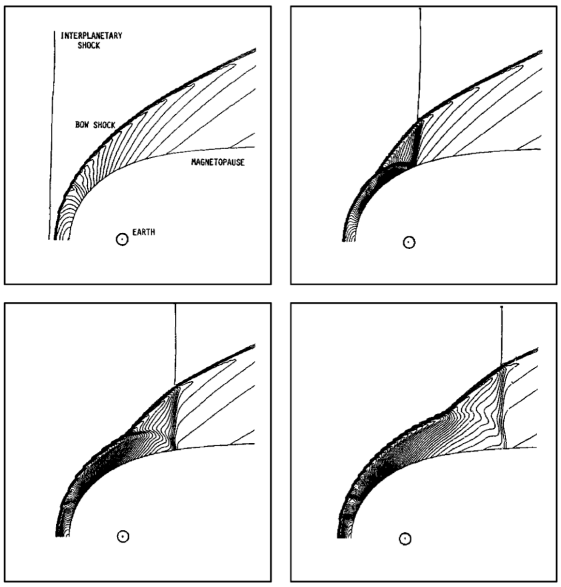

Figure 1.20: Plasma pressure contours in the terrestrial magnetosheath during passage of an interplanetary shock as predicted by *Spreiter and Stahara* (1992) modeling. Adapted from *Stahara* (2002).

dicted arrival times in the MSH. They conclude that there is no clear dependence of the arrival times on the spacecraft separation from the Sun-Earth line indicating no systematic deformation is present in the pressure front surface.

However, the difference between the shock parameters in the magnetosheath and those in the solar wind have also been reported. For example, *Zhuang et al.* (1981) analyzed propagation of three IP shocks for which measurements of ISEE 1, 2, and 3 were available in the solar wind and magnetosphere. Using the *Zhuang and Russell* (1981) model of the magnetosheath, they concluded that an IP shock front does not propagate as a plane in the magnetosheath: The different elements of the front have different velocities and orientations.

More recently, *Villante et al.* (2004) examined 20 fast forward IP shocks detected by Wind in the solar wind in order to determine propagation speeds of shock-associated disturbances in the magnetosheath. They found the propagation velocity for shock-associated disturbances through the magnetosheath to be $\sim$1/3–1/4 of the solar wind shock speed. However, their study is based on the solar wind and ground observations only, assuming a transit time between the magnetopause and the Earth's surface of $\sim$1–2 min.

Chapter 2

The aims of the thesis

The interplanetary shocks and other types of discontinuities are a distinct feature of the solar wind. The prediction how the disturbances propagate in the solar wind, how they are modified in the bow shock region and through the magnetosheath, and how they affect the Earth's magnetosphere is a key question of present magnetospheric physics. In this thesis, we discuss two closely related topics: (1) interaction of interplanetary magnetic field tangential discontinuities with the Earth's bow shock and properties of resulting hot flow anomalies, and (2) propagation of interplanetary shocks through the solar wind, their interaction with the Earth's bow shock and modification of their parameters in the magnetosheath.

We have chosen these two types of discontinuities (tangential discontinuity and IP shock) as typical representatives of the solar wind variations and due to their high geo-effectiveness. Tangential discontinuities are usually not accompanied by any significant plasma variation; however, their interactions with the Earth's bow shock lead to the formation of HFAs with a complex structure. IP shocks are precursors of the arrival of large structures of solar origin, such as CMEs and CIRs, thus the shocks are followed by regions of compressed magnetic fields and enhanced plasma densities which can cause geomagnetic disturbances (e.g., magnetic storms, and sub-storms) via interaction with the Earth's magnetic field.

Our study will be based on simultaneous observations of several spacecraft that operated as distant solar wind monitors (SOHO, Wind, ACE), or were located either in a close vicinity of the Earth's bow shock (IMP 8, Geotail, Interball-1/MAGION-4) or in the magnetosheath (Geotail, Interball-1/MAGION-4). For the study of IP shock propagation, we suppose to focus on analysis of events when the shock arrival is observed by at least four spacecraft in the solar wind and, assuming planar shock geometry, we could directly calculate global shock characteristics from the times of a shock arrival to a particular spacecraft. Since IP shocks are rather rare in the solar wind and suggested way of data processing requires multi-point observations, we will start with a survey of available solar wind and magnetosheath observations and create a database of observed shocks for a period from 1995 to 1999 when most of the mentioned spacecraft operated simultaneously.

Father, we plan to use the high-time resolution data of ion fluxes measured by the omnidirectional plasma sensor (VDP) onboard the Interball-1 spacecraft. To determine particular ion flow parameters (three components of the velocity vector, temperature, and

density), we have developed new methods based on a comparison of actual observations with model results of the instrumental response for various sets of ion flow parameters assuming an isotropic Maxwellian velocity distribution.

Chapter 3

Instrumentation and data processing

3.1 Spacecraft measurements in the solar wind and magnetosheath

Data from several spacecraft have been used in our study: Wind, ACE (Advanced Composition Explorer) and SOHO (Solar and Heliospheric Observatory) measured far upstream in the solar wind, while Geotail, IMP 8 (Interplanetary Monitoring Platform), and Interball-1/MAGION-4 observed either the solar wind plasma in the vicinity of the Earth's bow shock or the magnetosheath population.

Table 3.1 shows the spacecraft instruments used in the study and their time resolution: Wind magnetic field (*Lepping et al.*, 1995) and plasma (*Ogilvie et al.*, 1995; *Lin et al.*, 1995) instruments, ACE magnetic field (*Smith et al.*, 1998) and plasma (*McComas et al.*, 1998a) instruments, SOHO plasma instrument (*Ipavich et al.*, 1998), Geotail magnetic field (*Kokubun et al.*, 1994) and plasma (*Frank et al.*, 1994) instruments, IMP 8 magnetic field (ftp://nssdcftp.gsfc.nasa.gov/spacecraft_data/imp/imp8/mag/ (A. Szabo and R. P. Lepping, NASA GSFC)) and plasma (*Bellomo and Mavretic*, 1978) instruments, Interball-1 magnetic field (*Klimov et al.*, 1997; *Nozdrachev et al.*, 1998) and ion flux (*Šafránková et al.*, 1997) instruments, MAGION-4 magnetic field (*Ciobanu and Moldovanu*, 1995) and ion flux (*Šafránková et al.*, 1997) instruments.

Among the above listed spacecraft, Interball-1 has some advantages for our study: (1) trajectories of the spacecraft are suitable for study of interaction of solar wind discontinuities with the Earth's bow shock and their propagation in the magnetosheath because, being launched into a highly elongated polar orbit, Interball-1 passed through the magnetosheath twice per orbit lasting four days; (2) the spacecraft provided the highest time resolution of plasma and magnetic filed measurements.

There were two devices for plasma measurements onboard Interball-1 — ion energy spectrometer (CORALL) and ion flux detector (VDP). However, time resolution of CORALL measurements were $\sim$2 minutes and geometry of this device did not allow to determine solar wind parameters and thus we were forced to use VDP measurements.

Spacecraft	Region	Instrument / time resolution, s			
		Plasma		Magnetic field	
Wind	SW	SWE	93	MFI	3
		3DP	3		
ACE	SW	SWEPAM	64	MAG	16
SOHO	SW	CELIAS MTOF	30	———	
Geotail	SW, MSH	CPI	45	MGF	3
IMP 8	SW, MSH	PLA	60	MAG	15
Interball-1	SW, MSH	VDP	0.0625	FM-3/MIF-M	0.0625
MAGION-4	SW, MSH	VDP-S	0.125–1	SGR	0.25

Table 3.1: Spacecraft instruments for plasma and magnetic field measurements and their time resolutions. The spacecraft measured either in the solar wind (SW) or in the magnetosheath (MSH).

3.2 Ion flux measurements onboard Interball-1

We describe the VDP instrument and a way of data processing for determination of basic plasma parameters from measurements of the ion flux in several directions.

3.2.1 Omnidirectional plasma sensor VDP

The omnidirectional plasma sensor VDP (*Šafránková et al.*, 1997) was intended predominantly for investigation of the hot turbulent plasma population which is frequently found in the tail of the Earth's magnetosphere. The device was designed for determination of integral flux vector and integral energetic spectrum of ions and electrons in the 0.2–2.4 keV energy range.

For simultaneous measurements in all directions, the VDP device was equipped with six identical wide-angle Faraday's cups (FCs) (*Šafránková et al.*, 1995). Their axes form a three-dimensional orthogonal system (Figure 3.1). The axes of the FC0 and FC5 are parallel to the spin axis of the satellite, the FC0 being oriented towards the Sun. Unfortunately, measurements of two Faraday's cups (FC3 and FC5) cannot be used due to technical difficulties.

The configuration of a Faraday's cup is shown in Figure 3.2. It consists of a body, outer and inner diaphragms with grids, positive and negative control grids, a suppressor grid, and a collector. The size of the collector, diameters of apertures and distances between the grids are chosen so that the angular characteristics of the sensor have a triangular shape with a full-width of 135°. The entrance grid is connected with the Faraday's cup body (and accordingly with the spacecraft body) for the protection of the environmental space from influence of the device potentials. Two control grids are used for selection of the registered particles according to the energy and charge. The grid on the inner diaphragm is connected with the body to protect the collector from the influence of the negative control grid potential. The suppressor grid eliminates or diminishes photoelectron and secondary electron currents from the collector. It is supplied permanently with a negative voltage of -170 V. This potential exceeds considerably the possible energy of secondary electrons

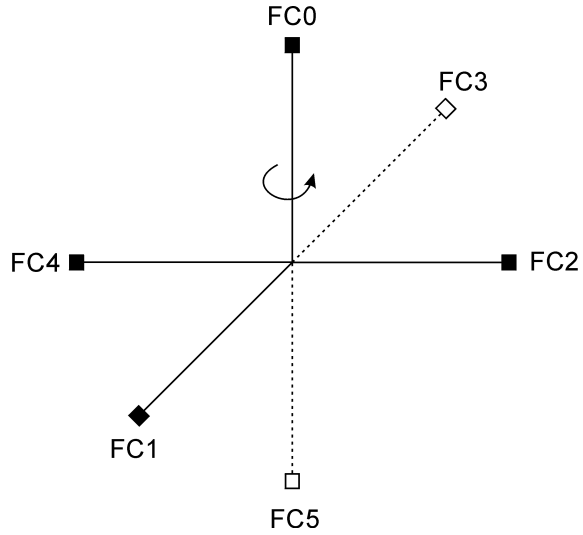

Figure 3.1: Configuration of the omnidirectional plasma sensor VDP. Faraday's cups FC3 and FC5 are inoperative.

and photoelectrons arising under the action of the solar ultraviolet (UV) radiation.

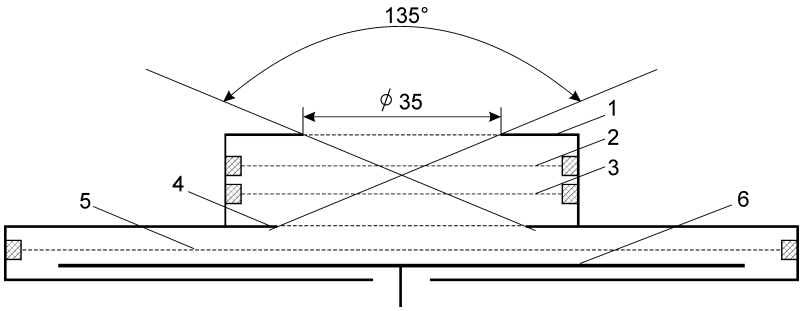

Figure 3.2: Geometry of a Faraday's cup: (1) an outer diaphragm with a grounded grid, (2) a positive control grid, (3) a negative control grid, (4) an inner diaphragm with a grounded grid, (5) a suppressor grid, (6) a collector.

The VDP device operates in the following modes:

- measurement of the sum of total ion flux and flux of electrons with energy greater than 2.4 keV;
- measurement of the sum of flux of electrons with energy greater than 0.17 keV and flux of ions with energy greater than 2.4 keV;
- measurement of the sum of the integral energy spectrum of ions in the range 0.2–2.4 keV and the flux of electrons with energy greater than 2.4 keV;
- measurement of the sum of the integral energy spectrum of electrons in the range 0.2–2.4 keV and the flux of ions with energy greater than 2.4 keV;

According to these modes, the control grids are supplied with potentials (relative to the body) shown in Table 3.2.

Operating mode	Positive control grid potential, kV	Negative control grid potential, kV
Ion flux	0	−2.4
Electron flux	+2.4	0
Spectrum of ion flow	step voltage +0.2/+2.4	−2.4
Spectrum of electron flow	+2.4	step voltage −0.2/−2.4

Table 3.2: Potentials on the control grids of a Faraday's cup for four operating modes.

For the measurement of the integral energetic spectrum of particles, the whole voltage range (0.2–2.4 kV) is divided equidistantly in logarithmic scale into 16 steps which are scanned each second.

The negative control grid of FC0 which is oriented towards the Sun is connected with the body to prevent the photoelectrons with energies up to 2.4 keV (i.e., considerably more than the potential of the suppressor grid) to come from it to the collector. Obviously, the suppressor grid also protects the collector from the current of any low energy electrons such as those from the internal surface of the sensor body and from the spacecraft body. However, there is some contribution to the collector current created by secondary electrons and photoelectrons from the suppressor grid itself. To reduce this current, the suppressor grid is designed to be as much transparent as possible. In this instrument the transparency of the suppressor grid is 0.95 and that of the others — 0.90.

To limit the light reflection from the collector towards the suppressor grid, the collector surface is rifled and coated with a special black nickel coat. This coat provides a reduction of the solar UV radiation reflectance at 120 nm to 6%. As the result, the photocurrent registered by the sensor with sunward orientation is reduced about 200–300 times in comparison with unprotected collector.

Figure 3.3 demonstrates examples of the magnetosheath ion fluxes measured by four Faraday's cups of the VDP device in two modes: "ion flux" and "spectrum of ion flow". As seen from the figure, there is a modulation of FC1, FC2 and FC4 fluxes with a period of about 120 s in both modes due to the rotation of the spacecraft. In the "spectrum of ion flow" mode, there is an additional 32-s modulation of all fluxes caused by the changing retarding potential on the positive control grid.

3.2.2 New methods for the determination of ion flow parameters

The ion fluxes, either total or integral spectrum, measured by four mutually perpendicular Faraday's cups can be used for the determination of ion flow parameters. The method is based on a comparison of actual observations with model results of the instrumental response for various sets of ion parameters assuming an isotropic Maxwellian velocity distribution.

For an isotropic Maxwellian velocity distribution, the ion flux measured by a Faraday's cup depends on ion bulk velocity vector, thermal velocity, and density. For Faraday's cups with no potential on the control grids, the ratio of the total ion fluxes measured by two sensors oriented in different directions depends on three parameters: direction of

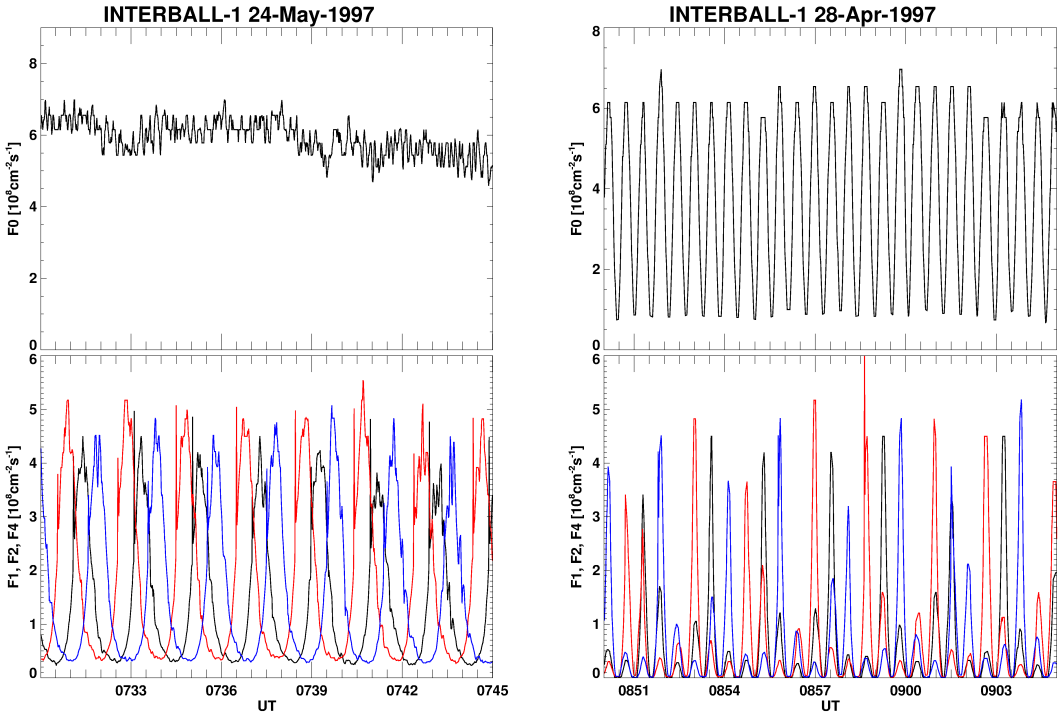

Figure 3.3: Magnetosheath ion fluxes measured by four Faraday's cups of the VDP device in two modes: "ion flux" (*left*) and "spectrum of ion flow" (*right*).

ion bulk velocity and ratio of ion bulk and thermal velocities. Since simultaneous measurements of four Faraday's cups are available, it is possible to calculate three independent ratios of ion fluxes, each depends on three parameters and these three parameters can be uniquely determined from total ion fluxes measured by the VDP device (e.g., *Zastenker et al.*, 2000). An example of the calculated parameters for a magnetosheath crossing is shown in Figure 3.4.

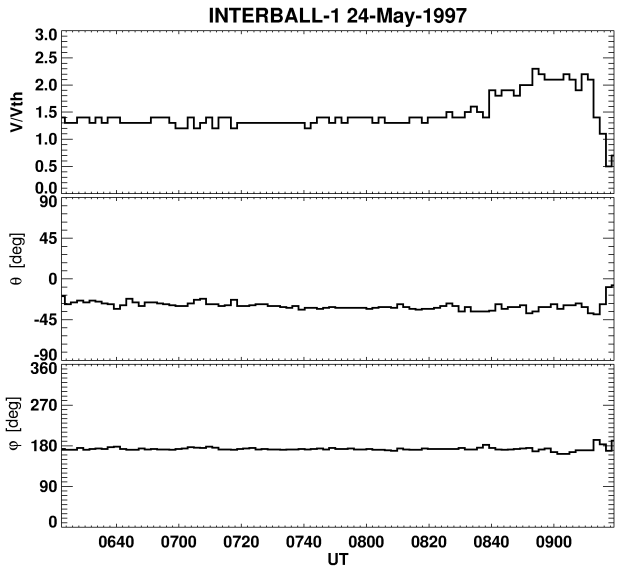

Figure 3.4: An example of the calculated ratio of ion bulk and thermal velocities (V/Vth) and two angles (θ and ϕ) that define the direction of the ion bulk velocity. θ is the angle between the ion flow vector and XY plane, being positive for the positive Z component; ϕ is the angle between the positive X direction and the projection of the ion flow vector onto the XY plane counted toward the positive Y direction.

However, a potential of -2.4 kV on the negative control grid which is applied for high-energy electron cutoff affects trajectories of ions with different magnitudes of bulk velocity and the same ratio of bulk and thermal velocities in a different way. This fact allows us to calculate the ion bulk velocity vector (three components), temperature, and density. Having these five parameters, five independent measurements are required. Since only four measurements at each particular time are available, we used the spacecraft spin and added a virtual Faraday's cup. We placed this virtual detector into the plane perpendicular to the spacecraft spin axis (i.e., in the plane of FC1-FC4 detectors) and declined it by 45° from the nearest one. As measurements of this detector, either the data of the FC2 detector shifted ahead or the data of the FC4 detector shifted back can be used. These two possibilities are denoted as FC V1 and FC V2, respectively in Figure 3.5. Since the satellite spin period is $\sim$120 s, the time difference among measurements is $\sim$15 s and it limits achievable time resolution.

This method gives good results for gradually changing plasma flow but non-simultaneous measurements of detectors can be a source of errors in the cases of sharp discontinuities. For this reason, we compute two sets of parameters using virtual detectors FC V1 and FC V2. If their values differ less than 30%, we use the mean and discard the results in other cases. Nevertheless, a careful inspection of the input data and definition of ap-

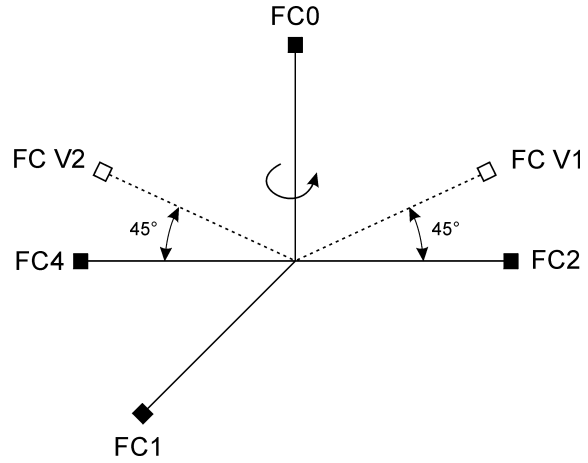

Figure 3.5: Faraday's cups used for determination of ion flow parameters. FC V1 and FC V2 are virtual Faraday's cups.

propriate intervals allow us usually to estimate the flow parameters on both sides of sharp discontinuities. An example of the five parameters determined inside a hot flow anomaly is shown in Figure 3.6.

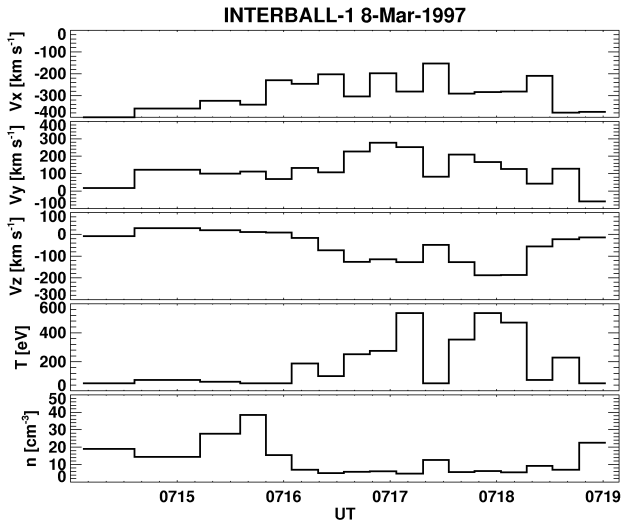

Figure 3.6: An example of the calculated ion bulk velocity vector (Vx, Vy, Vz), temperature (T) and number density (n) in the "ion flux" mode.

The changing potential on the positive control grid which is applied in the "spectrum of ion flow" mode can be used for a more accurate determination of solar wind plasma parameters. Having three parameters (V/Vth, θ and ϕ) from simultaneous measurements of total ion fluxes by four Faraday's cups, we can use the energy spectrum measured by FC0 which is oriented towards the Sun for determination of the ion bulk velocity, and hence the ion thermal velocity and density. Figure 3.7 shows an example of the parameters determined by such method for a magnetosheath crossing.

All above described methods are available for high ion-temperature regions like hot flow anomalies or the magnetosheath when all Faraday's cups measure sufficient ion cur-

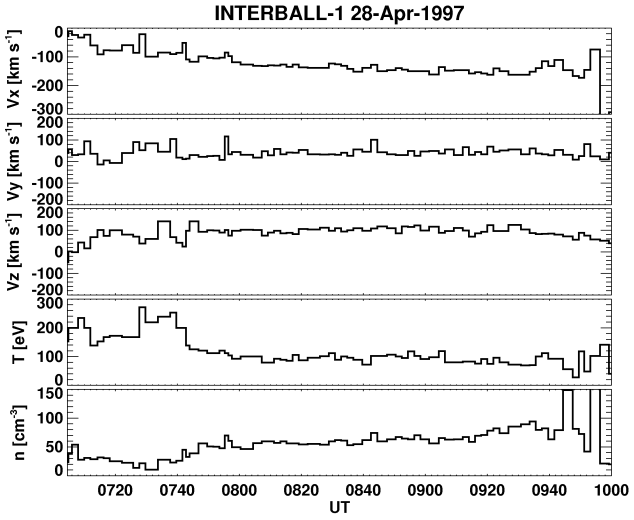

Figure 3.7: An example of the calculated ion bulk velocity vector (Vx, Vy, Vz), temperature (T) and number density (n) in the "spectrum of ion flow" mode.

rents. From the Faraday's cup geometry, we can derive that a reliable determination of plasma parameters can be obtained when the ratio of bulk to thermal velocities is less than 5. Since the ratio is usually above 10 in the solar wind, we are limited to the measurements of FC0 which provides the value of the total ion flux under these conditions.

3.3 Improvement of time resolution of solar wind parameter measurements

We used the advantages of a high-time resolution of ion flux measurements by Faraday's cups and a possibility to compute plasma parameters from them to develop a small fast monitor. We suppose that this solar wind monitor will be placed on the SPECTR-R spacecraft that will be launched in October 2007 into a highly elliptical orbit with apogee $\sim$350 000 km and perigee $\sim$10 000 km. The main goal of the project deals with astrophysical observations but simultaneously it represents a good platform for a solar wind monitoring because it will spend there $\sim$8 days out of the 9-day orbit. As follows from expected orbit, the small fast solar wind monitor would be designed for measuring in wide ranges of solar wind velocities (from 300–750 km/s), temperatures (from 1 to 30 eV), and densities (from 1–200 particles in cm^{-3}) assuming the angle of incidence up to 20°. A preliminary calculation of the method shows that the suggested system of Faraday's cups can provide reliable data with $\sim$8 Hz of a time resolution. Besides the solar wind monitor, the project will be equipped with the AC/DC magnetometer, energetic particle detectors, and the detector which will define an actual orientation in the Earth-Sun line.

3.3.1 Configuration of a small fast solar wind monitor for the SPECTR-R project

The device is described in detail in *Koval et al.* (2005a) [A1]. Suggested solar wind monitor consists of six Faraday's cups: three Faraday's cups are oriented towards the Sun and they are dedicated to determine the ion bulk velocity magnitude, temperature, and density from three points of the velocity distribution function assuming an isotropic Maxwellian distribution; other three Faraday's cups are declined on 20° from the sunward direction and serve for a calculation of the ion-flow direction.

Geometry of a Faraday's cup is shown in Figure 3.8. The diaphragm diameters and other dimensions of the Faraday's cups were chosen to provide a measurable ion current for all possible angles of incidence and in a full range of expected solar wind parameters in regions encountered by the spacecraft, i.e., in the solar wind and nightside magnetosheath.

The Faraday's cups are equipped with four grids (see Figure 3.8): grounded grids cover the windows in both diaphragms; a positive control grid is placed at an equidistance from outer and inner diaphragms; and a suppressor grid lies between the inner diaphragm and a collector. The grounded grids are used for an elimination of an internal electric field outside Faraday's cup. The purpose of the positive control grid and its operating mode are discussed in detail below together with the method of determination of solar wind parameters. The suppressor grid is powered by a negative potential of ~ -300 V. This potential returns back photoelectrons emitted from the collector by solar UV radiation as well as solar wind electrons. The potential value is sufficient for accurate measurements in a plasma with the electron temperatures up to $\sim$100 eV, i.e., for the solar wind and magnetosheath.

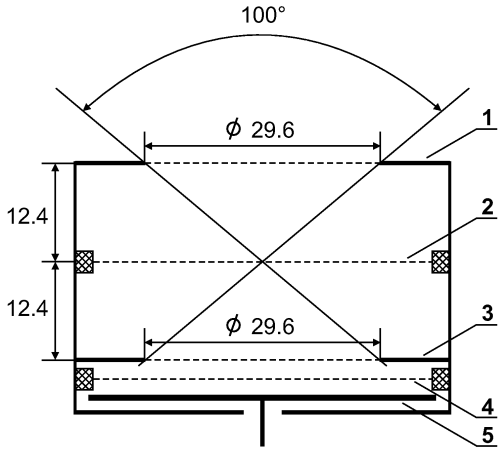

Figure 3.8: Geometry and dimensions of a Faraday's cup: (1) an outer diaphragm with a grounded grid, (2) a positive control grid, (3) an inner diaphragm with a grounded grid, (4) a suppressor grid, (5) a collector.

3.3.2 Determination of solar wind parameters

As was noticed in Section 3.2.2, for an isotropic Maxwellian velocity distribution, three independent ratios of total ion fluxes measured by Faraday's cups uniquely define the

ion-flow direction and the ratio of the bulk and thermal velocities. For this purpose, we suppose to use the fluxes measured by a Faraday's cup oriented towards the Sun and by three declined Faraday's cups. For measurements of the total ion fluxes, the control grid potentials are set to zero for these Faraday's cups.

The system for determination of the solar wind velocity and temperature uses the sunward oriented Faraday's cup from aforementioned set and two other Faraday's cups supplied with positive voltages. Figure 3.9 shows theoretical dependences of normalized collector currents on the control grid potential for an angle of incidence of 0° and different values of both thermal and bulk velocities. The calculations were made under assumption of the 95% proton and 5% alpha particle content and an isotropic Maxwellian velocity distribution with equal thermal velocities for both ion species. It can be seen that these dependences are close to linear in the range between 40% and 70% of the total ion current. Moreover, the influence of alpha particles on the velocity distribution is negligible in this range. Therefore, we will adjust the deceleration potentials of two sunward Faraday's cups to receive 0.4 and 0.7 fractions of the integral ion current measured by the sunward Faraday's cup without any decelerating potential. These control grid potentials together with the previously determined ion-flow direction allow us to calculate the ion bulk and thermal velocities. Finally, the ion density can be obtained by taking into account the value of the integral ion current. A preliminary computer modeling shows that the achievable time resolution is at least 8 Hz if all currents and grid voltages are measured with the 32 Hz rate.

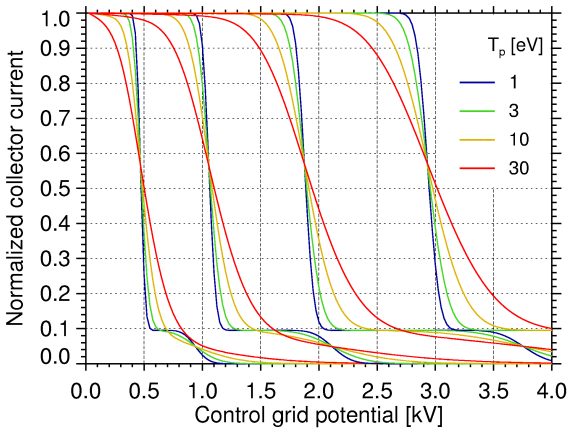

Figure 3.9: Dependences of a normalized collector current on the control grid potential for an angle of incidence of 0° and different values of the ion bulk velocity (300, 450, 600, 750 km/s — sets of curves from left to right) and proton temperature (1, 3, 10, 30 eV).

Characteristics shown in Figure 3.9 were calculated under an assumption of homogenous electric fields inside a Faraday's cup. However, wires of the control grid and grounded walls significantly affect the shape of the electric field, and hence trajectories of charged particles, inside the Faraday's cup. Influences of the finite Faraday's cup dimensions and grid spacing on the measured ion fluxes are discussed in *Koval et al.* (2005a) [A1].

During 2005, an engineering model was prepared (Figure 3.10) and first tests in a vacuum chamber were carried. These tests have shown that the noise level on the am-

plifier output is small enough and it allows us to decrease the entrance windows of those Faraday's cups designed for determination of the plasma velocity and temperature. The Faraday's cups with smaller windows exhibit the angular characteristics that are more appropriate for their tasks. The main advantage is that these characteristics are flat in a range of angles of incidence as can be seen from Figure 3.11. This figure shows the characteristics of the Faraday's cups with small (20 mm) and large (29.6 mm) entrance windows.

Figure 3.10: A photo of the solar wind monitor.

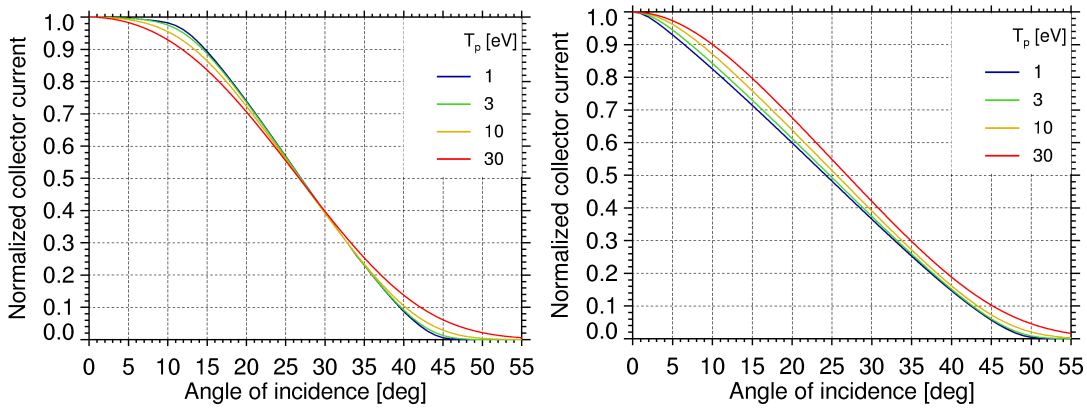

Figure 3.11: Angular characteristics of a sunward oriented Faraday's cup with the outer diaphragm diameter of 20 mm (*left*) and a declined Faraday's cup with the outer diaphragm diameter of 29.6 mm (*right*) for an ion bulk velocity of 400 km/s and proton temperature of 1, 3, 10, and 30 eV.

Finally, we would like to point out that the suggested device has several advantages. The application of six simple and similar Faraday's cups decreases the cost and increases the reliability. We expect that all sunward oriented Faraday's cups will be equipped with high voltage supplies and thus they can replace each another. Since only five independent measurements are required for a full determination of five parameters (density, temperature, and three components of the velocity vector), the device will be fully operable even after a breakdown of any single Faraday's cup.

Chapter 4

Particle flows in hot flow anomalies

This chapter presents the results of the study of HFAs where we used our methods of ion flow parameter calculation from ion fluxes (see Section 3.2.2) first.

Despite the fact that a significant progress in an HFA structure and gradual evolution studies was made, there are many problems in our understanding. Among them: (1) conditions that lead to the ion flux enhancement on both or only one edge of HFA, (2) a nature of double HFA formation, (3) the distinction in influence of a motional electric field oriented towards the IMF TD plane on both or only one side on an HFA formation, (4) the relationship between the deflected particle flow inside HFA and orientation of the original IMF TD.

In order to find out a relationship between the ion flow direction inside HFA cavities and orientations of IMF TDs, we have analyzed three HFAs in Interball-1/MAGION-4 solar wind measurements (*Koval et al.*, 2005b) [A2]. One of these HFAs for which the plane of the corresponding TD is almost parallel to the XY plane is described below in detail. For such orientation of the discontinuity plane, the flow direction in the discontinuity frame of reference coincides with the flow direction in the spacecraft frame of reference and can be estimated with a high time resolution.

On May 20, 1996, Interball-1 registered an HFA-like event in the vicinity of the bow shock at (14, 1.8, -4.7) R_E in the GSE coordinate system. Figure 4.1 presents Interball-1 ion fluxes and magnetic field. The observed event can be distinguished in Interball-1 measurements as two sharp jumps of the magnetic field strength (at $\sim$2322 and $\sim$2328 UT) from about 5 to $\sim$27 nT (Figure 4.1c). The region bounded by these enhancements exhibits a very strong ion flow observed by FCs oriented perpendicularly to the Sun-Earth line (Figure 4.1b), whereas the anti-sunward ion flow (Figure 4.1a) is highly depressed. The comparison of magnetic field components prior and after the event reveals that although the magnetic field strength remained nearly unchanged, the vector rotated on a large angle.

During the studied time interval, Wind monitored the solar wind and IMF conditions far upstream at (113, -29, -5.2) R_E. Its IMF and plasma measurements are shown in three bottom panels of Figure 4.1. The considered time interval does not contain any sharp change in the solar wind dynamic pressure confirming our suggestion of an IMF origin of the event. Moreover, the similarity of Interball-1 measurements after the event with those of Wind following a distinct discontinuity at 2258 UT suggests that this discontinuity can be considered as a cause of the observed disturbance. We marked this discontinuity with

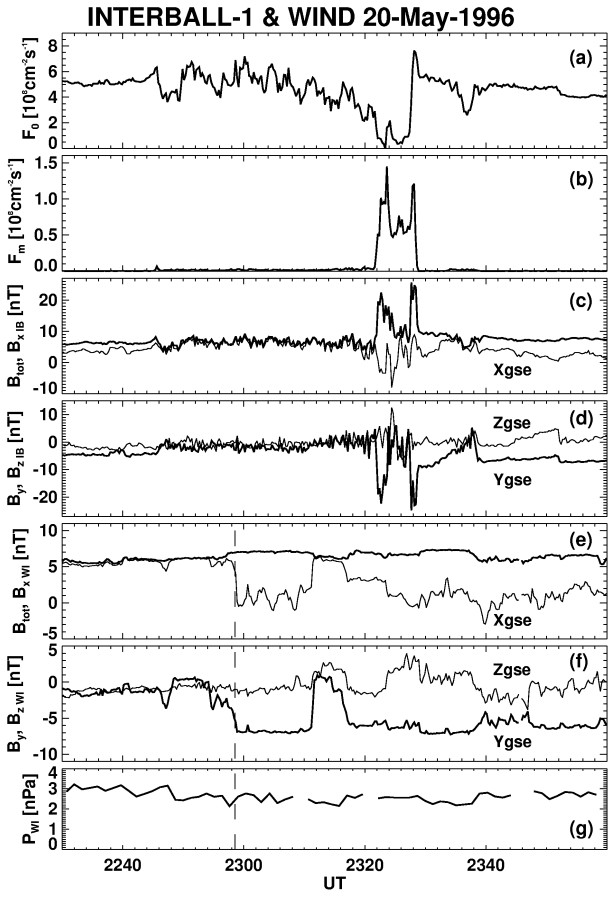

Figure 4.1: A summary plot of the solar wind HFA observed by Interball-1 and IMF TD observed by Wind. (a) The F_0 (Interball-1 ion flux in the anti-sunward direction), (b) F_m (Interball-1 ion flux in the plane perpendicular to the Sun-Earth line), (c) $B_{tot\ IB}$ (Interball-1 magnetic field magnitude), $B_{x\ IB}$, (d) $B_{y\ IB}$, $B_{z\ IB}$ (Interball-1 magnetic field components), (e) $B_{tot\ WI}$ (Wind magnetic field magnitude), $B_{x\ WI}$, (f) $B_{y\ WI}$, $B_{z\ WI}$ (Wind magnetic field components), (g) P_{WI} (Wind dynamic pressure).

a vertical dashed line in Figure 4.1.

The normal of the discontinuity calculated from the WIND data by the cross product of the magnetic field vectors on both sides of the discontinuity is $\boldsymbol{n}$=(0, 0.14, -0.99). A motional electric field is oriented towards the plane of the discontinuity on one side. The intersection of the TD plane with and projections of magnetic field vectors onto the XZ plane are shown in Figure 4.2. The arrows denoted as $\boldsymbol{B}_1$ and $\boldsymbol{B}_2$ show the projections of magnetic field vectors observed before and after the event. Note that the B_y component which cannot be seen in this projection was a principal component after the event and thus the full magnetic field vector was nearly parallel to the estimated discontinuity plane.

Using the method for the determination of ion flow parameters described in Section 3.2.2, we have calculated the ratio of bulk to thermal velocities (V/V_{th}) and two angles (θ and ϕ) that define the ion flow direction. Figure 4.3 (panels c, d, e) presents these parameters with 1-s time resolution for the time interval corresponding to the discontinuity. One can clearly see a sharp drop in a value of V/V_{th} from more than 4 to less

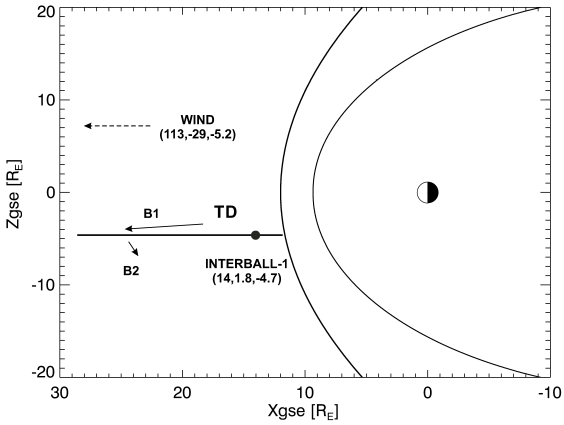

Figure 4.2: Intersection of the TD plane with and projections of magnetic field vectors onto the XZ plane.

than 1 (core region) and simultaneous significant changes of the ion flow direction at the discontinuity boundaries as well as along the core region.

Since the plane of the discontinuity is almost parallel to the XY plane, we can neglect its motion along the bow shock surface. Thus, we can calculate the angle (α) between the plane of the discontinuity and the ion flow direction with 1-s time resolution (Figure 4.3f). A positive value of the angle corresponds to the southward, while a negative value to the northward ion flow. We can observe that the ion flow is rather deflected from the discontinuity plane with an angle up to 70° which is roughly tangential to the bow shock surface at the leading edge, while is almost aligned with the plane at its trailing edge. The core region (2324:30-2327:20 UT) is characterized by a moderate value of this angle that does not exceed 20°.

Although the IMF TD has all features required for a HFA creation, the resulting disturbance is not a typical HFA. It is bounded by magnetic field enhancements (Figure 4.3b) on both sides but only the trailing edge has characteristics of the fast shock. The compression of the field on the trailing edge is accompanied with compression and slight heating of the plasma. The V/Vth ratio is about 2.6 and the total ion flux is enhanced by a factor of 1.5 with respect to the undisturbed solar wind observed after 2328:30 UT. On the other hand, the space with enhanced magnetic field on the leading edge of the disturbance (2322-2324 UT) is filled with hot and tenuous plasma similar to that in the core region. The only difference between these two plasmas is the flow direction. It is deflected from the discontinuity plane towards south inside the enhancement, whereas northward declination characterizes the core region. However, the ratio of bulk to thermal velocities is very low and indicates nearly standing plasma in the core region.

Our analysis of the flow directions in the described HFA and two other HFAs (*Koval et al.*, 2005b) [A2] reveals that the deflection from the original solar wind velocity starts in bounding density enhancements if they exhibit fast shock features. The flow direction inside the core region can be determined only approximately because the bulk speed is comparable or even smaller than the thermal speed. Nevertheless, the flow velocity lay nearly in the discontinuity plane in all analyzed events. The declinations up to $\pm 20°$ can be probably attributed to the fluctuations of the IMF direction changing slightly the

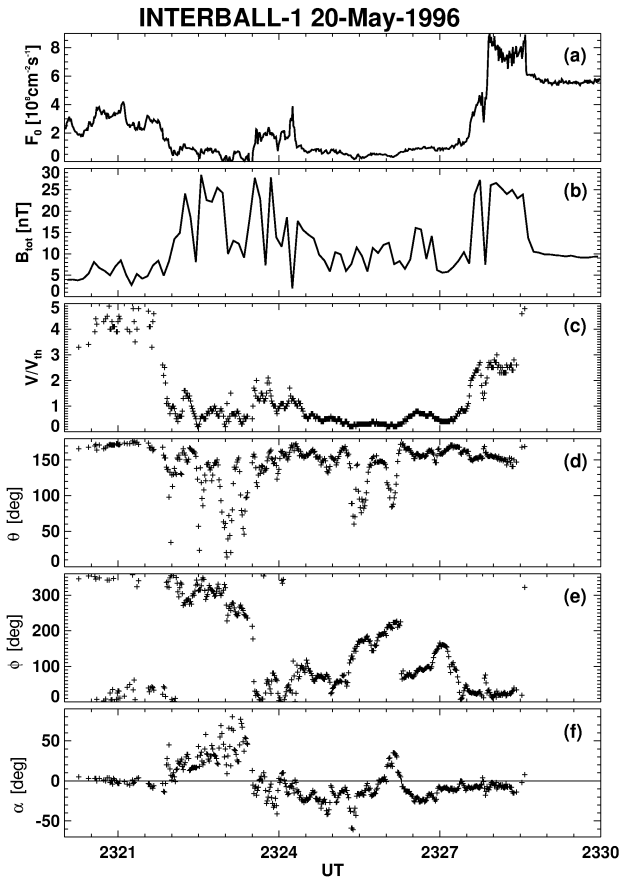

Figure 4.3: Interball-1 HFA observations: (a) F_0 (ion flux in the anti-sunward direction), (b) B_{tot} (magnetic field magnitude), (c) V/V_{th} (ratio of bulk to thermal velocities), (d) θ (angle between the ion flow vector and positive X direction), (e) ϕ (angle between positive Y direction and the projection of the ion flow vector onto the YZ plane counted toward positive Z direction), (f) α (angle between the ion flow vector and the plane of the discontinuity in the discontinuity frame of reference).

normal of the discontinuity plane. This flow carries a large amount of plasma in direction different from that of the undisturbed solar wind. However, this flow originates and should be terminated in the solar wind. One would expect to see a kind of transient process at these point but none of analyzed cases exhibits such features. It suggests that the HFA cavity is probably highly elongated in the direction of the discontinuity plane. A highly elongated shape can explain very different duration of HFA observations. HFA is crossed by the satellite in an arbitrary direction and the velocity of a HFA motion with respect to the bow shock is given by the orientation of the seed TD. The duration of HFAs in satellite observations can range from seconds to tens of minutes.

Finally, we could summarize that our results bring a new knowledge about the HFA topology and these results are consistent with recent four-point observations of hot flow anomalies by the Cluster spacecraft (*Lucek et al.*, 2004).

Chapter 5

Propagation of interplanetary shocks through the solar wind and magnetosheath

In this chapter, we present some peculiarities of IP shock propagation through the solar wind and magnetosheath. We start with a distinct example of an IP shock evolution and proceed with comparisons of IP shock parameters and magnetic field and plasma parameters across a shock in the solar wind and magnetosheath. The spacecraft observations are accompanied by the global 3-D MHD BATS-R-US modeling and a local magnetosheath modeling and we discuss the model abilities to reproduce the observed features.

The presented and many other examples of observations of IP shock passing were chosen from a database that we created before analyzing of single events. During the time interval from 1995 to 1999, we have identified about 120 IP shocks, most of them being of a fast forward type.

5.1 Modification of an interplanetary shock in the solar wind and magnetosheath

We briefly discuss an example that demonstrates possibility of evolution of an IP shock while propagating through the solar wind and its transformation into another type of the MHD shock after an interaction with the Earth's bow shock (*Koval et al.*, 2004) [A3].

On January 31, 1998, Wind and ACE identified an IP shock far upstream in the solar wind (Figure 5.1 where projections of spacecraft locations onto the ecliptic plane are presented). The shock was registered first by Wind at 1553:46 UT and latter by ACE at 1600:31 UT. Wind and ACE observations corresponding to these times are presented in left panels of Figure 5.2. The arrival of the shock can be clearly seen in magnetic field and plasma data. It is characterized by an abrupt increase of the IMF magnitude as well as the solar wind speed and density. According to changes of these parameters, the discontinuity can be classified as a fast forward shock. It propagated through the solar wind to the Earth's bow shock vicinity where IMP 8 identified a corresponding disturbance (two left bottom panels in Figure 5.2). However, the profile of the disturbance observed near the Earth's bow shock differs significantly from that of the initial shock. Propagating through

the solar wind, the shock evolves into a slow IMF rotation which is registered by IMP 8. A small-amplitude sharp IMF change at 1642 UT is supposed to be a signature of the initial shock observed at L1.

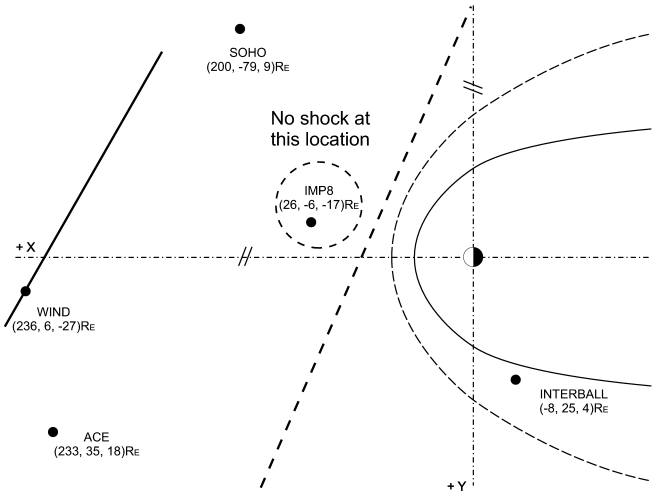

Figure 5.1: The projections of spacecraft locations onto the ecliptic plane and shock plane estimations. The global shock orientation calculated from the times of the shock arrival to four spacecraft is denoted by a dashed line while a local shock orientation at the Wind location calculated using Rankine-Hugoniot conservation equations is denoted by a heavy line.

The IMF rotation interacts with the Earth's bow shock and produces a new shock-like discontinuity in the magnetosheath where it is observed by Interball-1 (Figure 5.2, right panels). Two right top panels in Figure 5.2 show magnetic field measurements corresponding to the discontinuity arrival. The discontinuity is clearly identified by a very sharp increase of the magnetic field magnitude at 1649:41 UT. The other right panels in Figure 5.2 present the ion anti-sunward flux, proton number density, and speed as well as ion and electron spectra. Since the increase of the magnetic field magnitude is accompanied by the decrease of the density, the discontinuity in Interball-1 data exhibits the features of a slow reverse shock despite the fact that the initial solar wind shock has all attributes of a fast forward shock.

As a conclusion, we could summarize according to (*Koval et al.,* 2004) [A3] that the shock observed far upstream evolves into a slow IMF rotation when propagating towards the Earth's bow shock. This IMF rotation interacts with the Earth's bow shock and produces a new shock-like discontinuity in the near-tail magnetosheath that can be classified as a slow reverse shock. The predicted time of the shock arrival to the magnetosheath location calculated from the solar wind shock parameters (*Koval et al.,* 2004) [A3] differs from that observed and this indicates that the IP shock is unlikely planar on the scale of spacecraft separation.

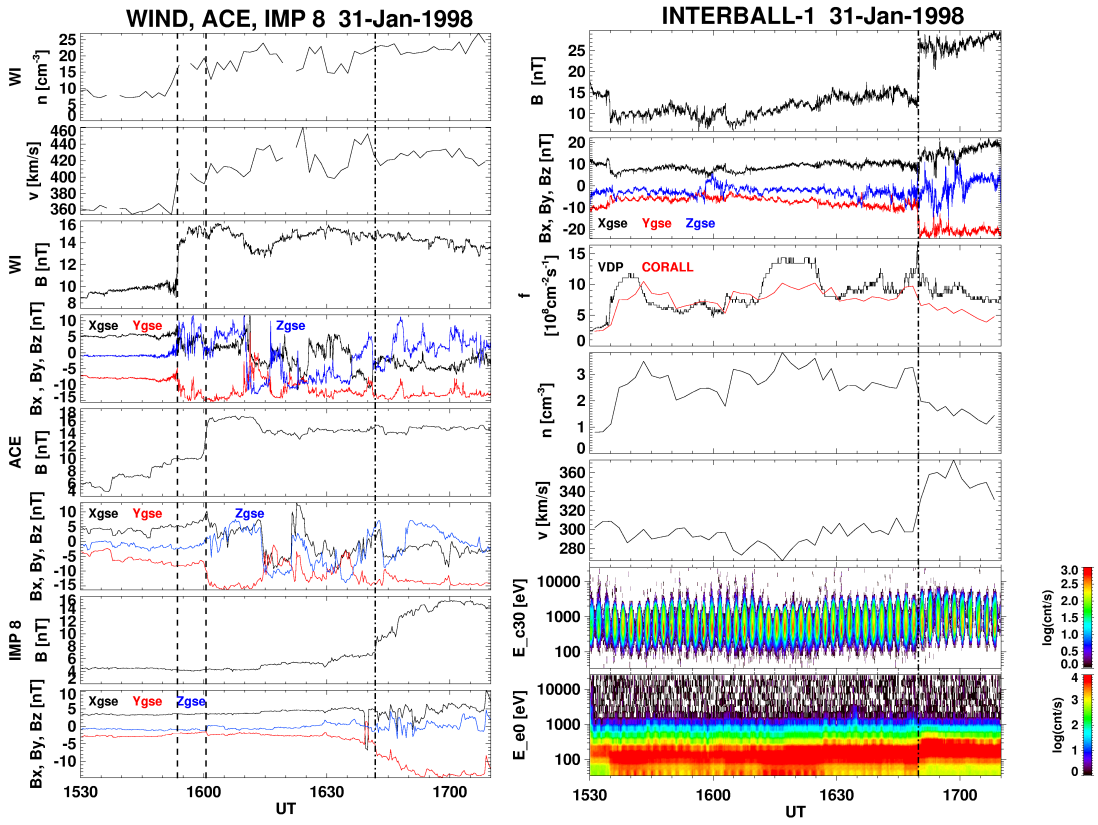

Figure 5.2: Observations of an IP shock by Wind (WI), ACE, and IMP 8 in the solar wind (*left*) and a corresponding disturbance observed by Interball-1 in the magnetosheath (*right*). Left panels: solar wind number density and speed measured by Wind and IMF measured by Wind, ACE, and IMP 8; Right panels: magnetosheath magnetic field, ion anti-sunward flux, proton number density and speed, ion and electron spectra.

5.2 Deformation of interplanetary shock fronts in the magnetosheath

Based on conclusion in the previous section, we discuss here possible deformations of an IP shock front in detail (*Koval et al.*, 2005c) [A4]. We present one example of an IP shock observed by four spacecraft in the solar wind and by one spacecraft in the magnetosheath. This case study is supplemented with a small statistical study of similar shocks and comparison of experimental data with a local MHD modeling.

5.2.1 Spacecraft observations

In late May 17 and early May 18, 1999, four spacecraft (SOHO, ACE, Wind, and Interball-1) were located in the solar wind and registered the passage of an IP shock; Geotail, in the magnetosheath, observed a corresponding shock-like discontinuity. Figure 5.3 shows the spacecraft geometry and model positions of Earth's bow shock (*Jeřáb et al.*, 2005) and magnetopause (*Petrinec and Russell*, 1996).

The ACE, Wind, and Interball-1 observations of the IP shock passage are presented

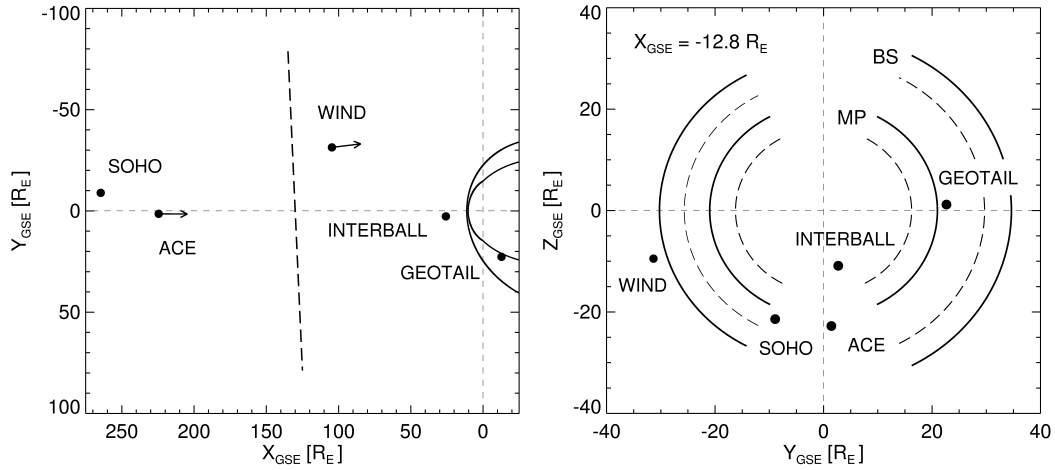

Figure 5.3: Projection of the spacecraft locations onto the ecliptic plane (a) and onto the YZ_{GSE} plane at $X = -12.8R_E$ (b). The *Jeřáb et al.* (2005) and *Petrinec and Russell* (1996) models were used to determine Earth's bow shock and magnetopause locations before (solid lines) and after (dashed lines) the shock arrival.

in Figure 5.4. Magnetic field magnitudes are shown from all three spacecraft; Wind magnetic field components and Wind 3DP 3-s temporal resolution proton number density and bulk velocity are also shown. The simultaneous jumps of the magnetic field magnitude, proton number density, and bulk velocity indicate that the observed IP shock is a fast forward shock. The three bottom panels in Figure 5.4 present the magnetic field magnitude, proton density, and bulk velocity measured by Geotail in the magnetosheath. As can be seen from the figure, the jumps of the magnetosheath parameters are not as sharp as in the solar wind. We discuss their behavior in detail in Section 5.3.

To study the propagation of the IP shock toward the magnetosheath, the shock normal orientation, and speed in the solar wind should be determined. We used magnetic field and plasma data from the ACE and Wind spacecraft and applied the Rankine-Hugoniot relations to determine the local shock normals and speeds. With measurements from four spacecraft located in the solar wind, we can also estimate the shock normal and speed as global shock parameters from the times of shock arrival at each spacecraft. Table 5.1 shows the derived shock parameters and Figure 5.3 shows the shock orientations: local shock normals computed from the Rankine-Hugoniot relations are denoted by arrows, while the global shock plane computed from the shock arrival times at each spacecraft is represented by a dashed line.

Technique	Shock Normal	Speed[1]	Speed[2]	Ma	Mf
ACE R-H	(-0.990, 0.005, 0.139)	440.2	99.8	2.28	2.15
Wind R-H	(-0.996, -0.087, -0.003)	450.4	99.9	2.46	2.30
4 S/C Timing	(-0.985, -0.063, -0.159)	429.8	83.8	2.01	1.89
Geotail R-H	(-0.961, 0.276, 0.000)	376.0	96.9	1.92	1.64

Table 5.1: Parameters of the IP shock (shock normals, speeds in km/s ([1] in Earth's and [2] plasma frames of reference), Alfvénic, and fast magnetosonic Mach numbers in the solar wind and magnetosheath.

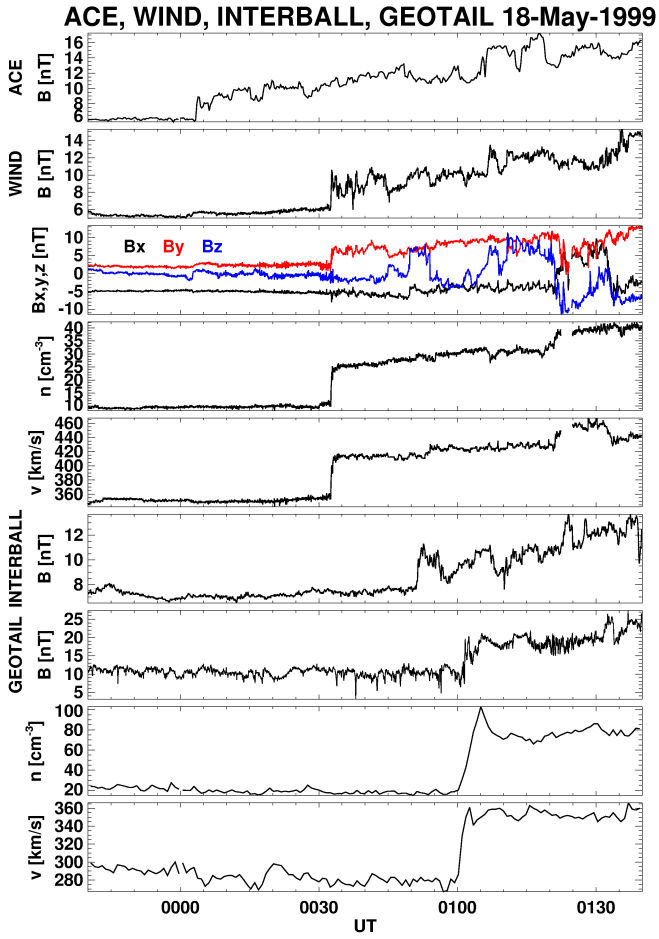

Figure 5.4: Observations of the IP shock passage by ACE, Wind, and Interball-1 in the solar wind and by Geotail in the magnetosheath. From top to bottom: ACE IMF magnitude, Wind IMF magnitude, and three IMF components, the Wind density and solar wind velocity, Interball-1 IMF magnitude, Geotail magnetic field magnitude, the density, and velocity.

The Rankine-Hugoniot relations can also be applied to the magnetosheath measurements of Geotail. The derived parameters are presented in Table 5.1. As seen from the table, the shock orientation in the magnetosheath differs significantly from that in the solar wind and the IP shock propagates much slower through the magnetosheath. However, the shock speeds in the plasma frame are almost equal in the solar wind and magnetosheath (Table 5.1). Therefore, the decrease of the shock speed in the magnetosheath can be attributed to a smaller bulk flow velocity.

In order to confirm the results of the shock deceleration in the magnetosheath, we have conducted a statistical study of a small number of similar shocks observed in the solar wind and magnetosheath.

The shock parameters in the solar wind can be determined from the magnetic filed and plasma parameters measured by a single spacecraft during the shock passage. However, we believe that the most reliable and least noisy parameters that can be derived from spacecraft observations are the time of the shock arrival at the spacecraft and the

coordinates of the spacecraft. The determination of shock parameters from the timing of observations requires the same shock be identified by at least four solar wind spacecraft and this requirement limits the number of IP shocks available for analysis. The number of shocks that can be studied is further decreased by the need to have at least one spacecraft operating in the magnetosheath as well as four in the solar wind.

Among the about 120 IP shocks observed in the solar wind for the time interval from 1995–1999, we have identified 10 fast forward shocks which satisfy these criteria. However, for each of these events, there is no a complete set of the magnetic filed and plasma parameters measured in the magnetosheath that precludes us from the direct comparison of shock parameters in the solar wind and magnetosheath. Therefore, we have computed the differences between the times predicted using the shock orientations and speeds calculated in the solar wind and the times of the shock arrivals in the magnetosheath.

Since the magnetosheath is relatively thin compared to the bow shock displacement due to pressure jumps across IP shocks, we divided all events into two groups which are determined by the magnetosheath observations. The first group contains events in which the spacecraft remains in the magnetosheath for a long time prior to and after the IP shock arrival (the event described above is an example). The second group contains events where the magnetosheath spacecraft crossed the bow shock within several minutes after the IP shock passed the spacecraft. Observations in the first group are likely closer to the magnetopause than those of the second group. The calculated delay times of IP shocks in the magnetosheath are plotted in Figure 5.5 as a function of the distance of the magnetosheath spacecraft from the magnetopause prior the IP shock arrival. The two groups of observations are distinguished by different symbols. Error bars reflect uncertainties of the shock determination due to the time resolution of the measurements onboard the spacecraft used for the particular calculation. The figure shows that almost all computed delays are positive which corresponds to deceleration of shocks. The only negative delay is small and belongs to the shock with the highest Alfvénic Mach number ($M_A \sim$5) in our set. However, the expected increase of the delay for the points closer to the magnetopause is not confirmed, perhaps because the number of points is small and their spread is large. Moreover, the magnetosheath observations significantly differ in the X_{GSE} coordinate.

5.2.2 Local MHD model of IP shocks in the magnetosheath

The observed shock deceleration in the magnetosheath disagrees with the gasdynamic model predictions of *Spreiter and Stahara* (1992). For this reason, we adapted the 3-D MHD model of solar wind flow around a blunt obstacle (*Samsonov and Hubert*, 2004) to allow for the propagation of a disturbance along the simulation box. A nonuniform grid system has been used with the resolution of about 0.3 R_E in the subsolar region. We have analyzed several runs where a discontinuity satisfying the fast shock jump conditions propagated toward the Earth (*Koval et al.*, 2005c) [A4]. Figure 5.6 illustrates the model results, showing the magnetic field intensity in the equatorial plane 3 and 4.5 minutes after a weak shock launch (see the Figure 5.6 caption for shock model parameters). The magnetic field strength is scaled to the undisturbed value at each point of the plot. The black line shows the location of the steepest gradient, which we presume is the bow shock. The IP shock can be easily distinguished on the plot as the boundary between the dark

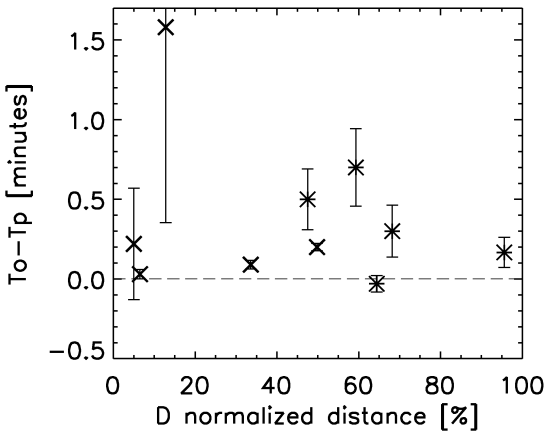

Figure 5.5: Differences between observed and predicted times ($To - Tp$) of IP shock arrival in the magnetosheath as a function of D, the ratio of the radial distance of the spacecraft from the model magnetopause (*Petrinec and Russell*, 1996) to the magnetosheath thickness (crosses – IP shock observations deep within the magnetosheath; asterisks — magnetosheath shock arrivals followed by bow shock crossings). For detail description of error bars see the text.

and light areas. The narrow light regions near the bow shock result from the bow shock displacement and our normalization because the magnetic field downstream of the IP shock is lower than that in the subsolar magnetosheath.

It can be seen from the figure that the shock propagates as a plane in the solar wind but its surface is curved in the magnetosheath. As one would expect, the shock speed just downstream of the bow shock is the same as that in the solar wind but it is significantly lower in the vicinity of the magnetopause. The time delay resulting from this deceleration is about $\sim$25 s after $\sim$3 minutes of IP shock propagation through the magnetosheath.

Because the results of the MHD model qualitatively agree with our previous observations (see Section 5.2.1 and Figure 5.5), we will compare measured and computed profiles of plasma density, velocity, and magnetic filed jumps across the IP shock in the next section.

5.3 Profiles of magnetic field and plasma parameters across a shock

For comparison of measurements with models we have chosen the already discussed event — May 18, 1999 (*Koval et al.*, 2005d) [A5].

Multi-spacecraft observations of the shock passage in the solar wind indicate that profiles of the magnetic filed and plasma parameters are similar at different locations there (see Figure 5.4). However, the magnetosheath profiles differ significantly from those observed in the solar wind: the jumps of the magnetosheath parameters are not as sharp as in the solar wind and there are overshoots of the magnetosheath proton number density and bulk velocity which are not observed in the solar wind.

In order to understand the difference between the behavior of the solar wind and

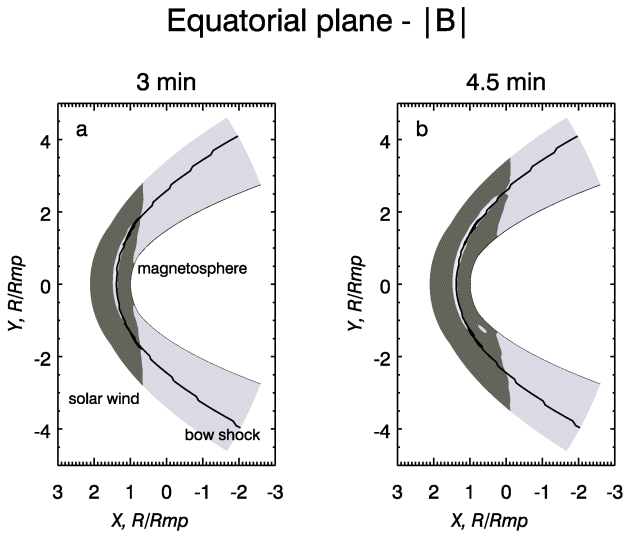

Figure 5.6: MHD modeling of an IP shock and its propagation in the MSH. Model shock parameters before the shock: $n = 5$ cm^{-3}; $V_x = 400$ km/s; $V_y = V_z = 0; T_i = 2.4 \cdot 10^5; |B| = 5$ nT; the angle in the X-Y plane = 45^o and the shock jumps: $B_2/B_1 = 1.24; n_2/n_1 = 1.2; T_2/T_1 = 2.7; V_{x2}/V_{x1} = 1.07$; the shock velocity = 568 km/s; and Alfvén Mach number = 3.4. Subscripts 1 and 2 correspond to upstream and downstream values of all parameters. The light area is before the shock ($B/B_0 \sim 1$) and the dark area is after the shock when $B/B_0 > 1$.

magnetosheath parameters, we simulated the magnetosheath parameters using two MHD models: the 3-D global BATS-R-US (Block-Adaptive-Tree-Solar wind-Roe-Upwind-Scheme) model (*Groth et al.*, 2000) and a 3-D local magnetosheath model (*Samsonov*, 2005). The comparison of the model predictions with observations is presented in Figure 5.7. The black solid lines show the Geotail data averaged to 15 and 50 s for the magnetic field and ion flow, respectively. The BATS-R-US computations are shown by dashed lines; red and blue lines show the two results from the local magnetosheath model — with solid (red line) and movable inner (blue line) boundaries. The comparison with the data reveals a good coincidence between the predicted and observed times of the shock passage, indicating that both models predict the observed deceleration of the shock in the magnetosheath. Differences in timing among models are small and they are attributed to the differing grid resolutions. The main difference between the models is the behavior of the IMF B_z component (last panel) that is nearly zero in the BATS-R-US computation. Profiles provided by the local magnetosheath model are more similar to the observations. The fluctuations observed in the post-shock interval are probably caused by the magnetopause reaction and thus their forms differ in the two versions of the local model.

All the modeled pre-shock magnetosheath values in Figure 5.7 are very close to those observed. The local magnetosheath model (both versions) gives a better match, probably because this model uses an approximation of the magnetopause surface obtained from the *Shue et al.* (1998) empirical model, whereas the BATS-R-US magnetopause is built self-consistently under simplified assumptions. The same is true for the post-shock interval.

The most interesting results were obtained for the interval immediately following the IP shock ramp (0100 – 0112 UT). All models predict an overshoot in the plasma velocity

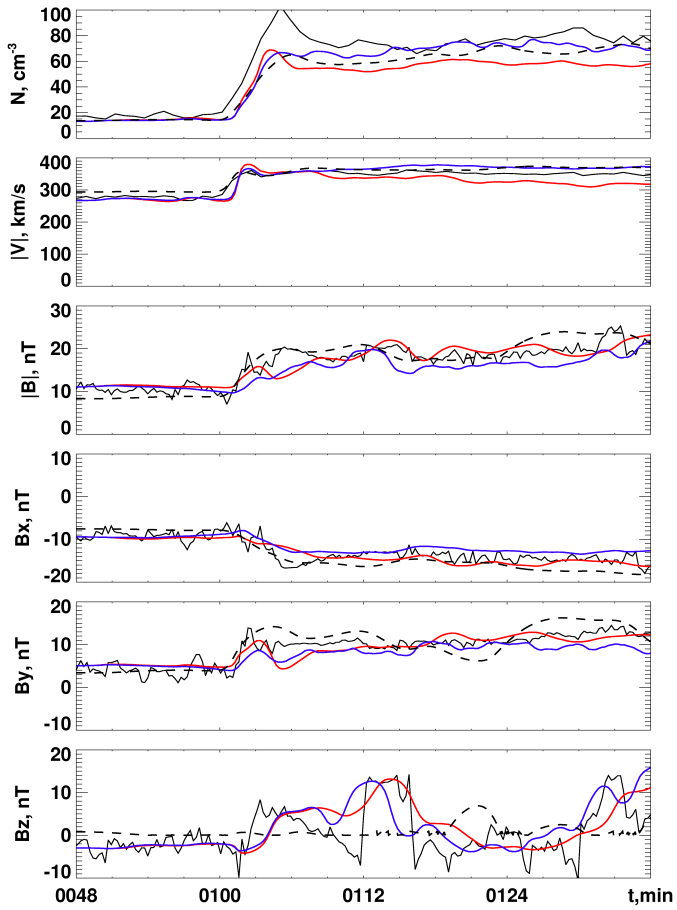

Figure 5.7: A comparison of Geotail magnetosheath observations with the BATS-R-US and a local magnetosheath model predictions (from top to bottom: densities, speeds, magnetic field magnitudes, and magnetic field components).

profile that is consistent with the observations. The observed density overshoot, however, is much larger than the model predictions. The most distinct overshoot is predicted by the local magnetosheath model with a solid obstacle (red line in Figure 5.7), whereas the overshoot is missing in the same model with the movable obstacle (blue line). This difference suggests that the presence of the overshoot is connected with the magnetopause reaction to the pressure pulse. The height of the overshoot is underestimated in all models and thus it may be connected with non-MHD effects.

Finally, we would like to conclude that both MHD models well reproduce the observed pre- and post-shock conditions as well as the steepness of the shock front in the magnetosheath. We did not find any significant differences in the plasma parameters predicted by the BATS-R-US model and two versions of local magnetosheath model. A comparison of two versions of the local model showed that the overshoot of the plasma density is caused by a delay in the magnetopause reaction to the increase of the upstream pressure. The good overall agreement between the measured and modeled data suggests that MHD effects dominate over kinetic effects even in the vicinity of the magnetopause.

Moreover, the fact that the times of measured and computed shock ramps coincide

confirms our hypothesis of shock front deformation in the magnetosheath. The estimated shock geometry for the discussed event is shown in Figure 5.8. The straight lines show the shock planes estimated from ACE, Wind, and from multi-spacecraft measurements at the time of the Geotail shock observation. The arrow at the Geotail location points along the shock normal computed from the Geotail data. The heavy curved line is an approximation of the IP shock front in the magnetosheath. That is consistent with observations as well as with MHD models. The shock orientation in the magnetosheath differs significantly from that in the solar wind and the IP shock propagates much slower through the magnetosheath.

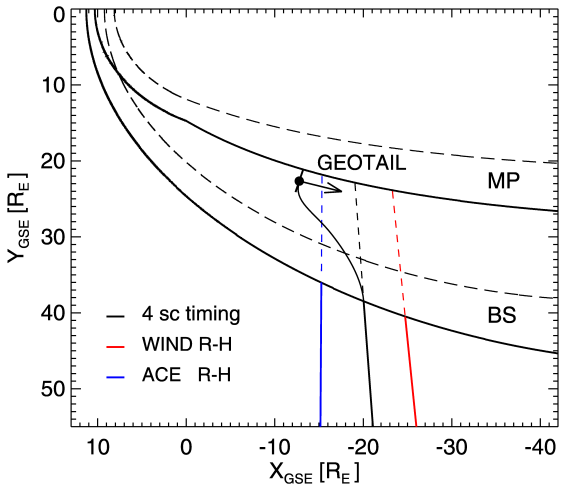

Figure 5.8: The shock orientation at Geotail in the magnetosheath and the corresponding solar wind shock orientations determined using different techniques. Solar wind shock positions correspond to the time of the shock arrival to the Geotail location.

In conclusion, we can compare our results with those previously reported. The gasdynamic model (*Spreiter and Stahara*, 1992) assumes a planar geometry for the incoming IP shock and predicts that transmitted magnetosheath pressure pulse will maintain planarity. This result is supported by the IMP 8 magnetosheath observations of *Szabo et al.* (2000, 2003). The authors did not find clear and systematic dependence in deformation of the pressure front surface.

By contrast, our results suppose a slight deformation of the IP shock front and these results are generally confirmed by MHD modeling. We think that there are several sources of this disagreement. We have used: (1) the best time resolution of plasma and magnetic field measurements accessible from all spacecraft, (2) the best (multi-spacecraft) method for determination of IP shock characteristics. Thus we obtained a smaller spread of shock arrival predictions than *Szabo et al.* (2003). We assume that this spread masks the shock deceleration which is rather small (Figure 5.5). Our comparison with MHD models suggests that magnetic forces play a non-negligible role in a shock propagation in the MSH.

Chapter 6

Conclusions

The thesis is devoted to the propagation of solar wind discontinuities through the solar wind and their interaction with the Earth's bow shock. Two main topics are discussed: (1) interaction of IMF tangential discontinuities with the bow shock and properties of resulting HFAs, and (2) propagation of IP shocks through the solar wind, their interaction with the bow shock and modification of their parameters in the magnetosheath.

To detect a motion and gradual evolution of solar wind structures, we used simultaneous multipoint observations by the Wind, ACE, SOHO, Geotail, IMP 8, and Interball-1/MAGION-4 spacecraft located in all crucial regions: far upstream in the solar wind, in the vicinity of the Earth's bow shock, and in the magnetosheath. Among these spacecraft, observations of Interball-1 were of a special interest due to a high-time resolution of magnetic field measurements and ion flux measurements by Faraday's cups of the omnidirectional plasma sensor (VDP) and due to suitable locations of the spacecraft in the magnetosheath or in the bow shock vicinity. To determine particular ion flow parameters (three components of the velocity vector, temperature, and density) from the ion flux measurements, we have developed new methods based on a comparison of actual observations with model results of the instrumental response for various sets of ion flow parameters assuming an isotropic Maxwellian velocity distribution. These methods are appropriate for high ion-temperature regions (e.g., magnetosheath) and allow to determine ion flow parameters with a high-time resolution up to 1 s.

We used the advantages of a high-time resolution of ion flux measurements by Faraday's cups and a possibility to compute plasma parameters from them to develop a small fast solar wind monitor (*Koval et al.*, 2005a) [A1]. It is supposed to be a part of the SPECTR-R project that will be launched in October 2007 into a highly elliptical orbit with apogee $\sim$350 000 km and perigee $\sim$10 000 km. The monitor, which consists of six similar Faraday's cups, is designed for measuring in wide ranges of solar wind parameters in regions encountered by the spacecraft, i.e., in the solar wind and nightside magnetosheath. A preliminary computer modeling shows that the suggested system of Faraday's cups can provide reliable data with $\sim$8 Hz of the time resolution.

The ion flow parameters computed from the measurements of the VDP instrument onboard the Interball-1 spacecraft were used for analysis of the relationship between the ion flow inside HFA cavities and orientations of an IMF tangential discontinuity (*Koval et al.*, 2005b) [A2]. Our results show that, beside the dominant plasma motion connected with the sweeping of the discontinuity, a significant velocity component directed along

the discontinuity can be found. This suggests a highly elongated shape of the HFA cavity. Such shape can explain very different durations of HFA observations which range from seconds to tens of minutes. The correlation length of particular HFA features (amplitude of bounding density enhancements, their durations, etc.) may be rather short; it is of the order of 1 R_E in our case. We also suggest that HFA which extends into the magnetosheath modifies locally downstream the Mach number and causes a local displacement of the bow shock.

The importance of an accurate determination of the parameters associated with the gradual evolution of IP shocks in the solar wind and their transmissions through the magnetosheath to the magnetosphere boundary led us to a detail study of propagation of an IP shock observed by multiple spacecraft in the solar wind and by at least one spacecraft located in the magnetosheath.

Multi-spacecraft observations of the shock passage in the solar wind indicate that the shock parameters are generally similar at different locations there and the corresponding magnetosheath shock-like discontinuity has characteristics of the same type of the MHD shock. However, we have also demonstrated a possibility of an IP shock evolution into a slow IMF rotation while propagating through the solar wind towards the Earth's bow shock and its transformation into another type of the MHD shock after an interaction with the Earth's bow shock (*Koval et al.*, 2004) [A3].

Among the multispacecraft observations, those events for which the passage of the shock is observed by at least four spacecraft located in the solar wind have significant advantages. Assumption of a planar shock geometry for these cases allows calculation of global shock parameters directly from the times of shock identifications by the particular spacecraft. In the time interval from 1995–1999, we have identified 10 IP shocks which satisfy this criterion. Our investigation of propagation of these shocks through the magnetosheath brings the evidence that IP shocks slightly decelerate there contrary to a gasdynamic prediction (*Koval et al.*, 2005c) [A4]. Therefore, we have modeled the propagation of IP shocks in the magnetosheath using two MHD models (the 3-D global BATS-R-US model (*Groth et al.*, 2000) and a 3-D local magnetosheath model (*Samsonov and Hubert*, 2004; *Samsonov*, 2005)) and showed that the observation of shock deceleration agrees with model predictions (*Koval et al.*, 2005c,d) [A4, A5]. Our MHD modeling suggests that the speed of the shock front propagation in the magnetosheath decreases from the bow shock toward the magnetopause and the front of the IP shock deforms. These MHD models also well reproduce magnetic field and plasma parameter profiles across the shock in the magnetosheath, although they are different from those in the solar wind (*Koval et al.*, 2005d) [A5]. The good overall agreement between measured and modeled profiles suggests that MHD effects dominate over kinetic effects in these interactions.

Finally, we would like to note that the propagation of solar wind discontinuities in the solar wind as well as in the magnetosheath is a complex problem and its investigation is not a simple task. Our results implicate that the assumption of the shock planarity in the magnetosheath should be abandoned and it makes this task even more complicated. Moreover, our as well as previous MHD modeling suggests that the interaction of an IP shock with the bow shock creates a train of new discontinuities and this fact would influence the IP shock arrival to the magnetopause. We think that our investigations contributed to a solution of these problems but much more remains for further studies.

Bibliography

Abraham-Shrauner, B. (1972), Determination of magnetohydrodynamic shock normals, *J. Geophys. Res.*, *77*, 736–739.

Abraham-Shrauner, B., and S. H. Yun (1976), Interplanetary shocks seen by AMES plasma probe on Pioneer 6 and 7, *J. Geophys. Res.*, *81*, 2097–2102.

Bellomo, A., and A. Mavretic (1978), Description of the MIT plasma experiment on IMP 7/8, in *Rep. CSR TR-78-2, Cent. for Space Res., MIT, Cambridge*, p. 51.

Berdichevsky, D. B., A. Szabo, R. P. Lepping, A. F. Viñas, and F. Mariani (2000), Interplanetary fast shocks and associated drivers observed through the 23rd solar minimum by Wind over its first 2.5 years, *J. Geophys. Res.*, *105*, 27,289–27,314, doi: 10.1029/1999JA000367.

Burgess, D. (1989), On the effect of a tangential discontinuity on ions specularly reflected at an oblique shock, *J. Geophys. Res.*, *94*, 472–478.

Burgess, D. (1993), Collisionless shocks, in *Introduction to Space Physics*, edited by M. G. Kivelson and C. T. Russell, Cambridge University Press.

Cairns, I. H., and J. G. Lyon (1995), MHD simulations of Earth's bow shock at low Mach numbers: Standoff distances, *J. Geophys. Res.*, *100*, 17,173–17,180, doi: 10.1029/95JA00993.

Ciobanu, M. I., and A. Moldovanu (1995), SGR 8 magnetometer for the Tail probe and Auroral probe satellites, in *INTERBALL Mission and Payload*, edited by Y. Galperin, pp. 230–232, CNES–IKI–RSA.

Dryer, M. (1973), Bow shock and its interaction with interplanetary shocks, *Radio Science*, *8*(11), 893–901.

Echer, E., W. D. Gonzalez, L. E. A. Vieira, A. Dal Lago, F. L. Guarnieri, A. Prestes, A. L. C. Gonzalez, and N. J. Schuch (2003), Interplanetary Shock Parameters during Solar Activity Maximum (2000) and Minimum (1995-1996), *Brazilian Journal of Physics*, *33*(1), 115–122.

Farris, M. H., and C. T. Russell (1994), Determining the standoff distance of the bow shock: Mach number dependence and use of models, *J. Geophys. Res.*, *99*, 17,681.

Feldman, W. C., J. R. Asbridge, S. J. Bame, M. D. Montgomery, and S. P. Gary (1975), Solar wind electrons, *J. Geophys. Res.*, *80*, 4181–4196.

Formisano, V. (1979), Orientation and shape of the earth's bow shock in three dimensions, *Planet. Space Sci.*, *27*, 1151–1161, doi:10.1016/0032-0633(79)90135-1.

Frank, L. A., K. L. Ackerson, W. R. Paterson, J. A. Lee, M. R. English, and G. L. Pickett (1994), The Comprehensive Plasma Instrumentation (CPI) for the Geotail spacecraft, *J. Geomagn. Geoelectr.*, *46*, 7–21.

Gonzalez, W. D., and B. T. Tsurutani (1987), Criteria of interplanetary parameters causing intense magnetic storms (Dst < -100 nT), *Planet. Space Sci.*, *35*, 1101–1109, doi: 10.1016/0032-0633(87)90015-8.

Gonzalez, W. D., B. T. Tsurutani, and A. L. Clúa de Gonzalez (1999), Interplanetary origin of geomagnetic storms, *Space Science Reviews*, *88*, 529–562.

Groth, C. P. T., D. L. De Zeeuw, T. I. Gombosi, and K. G. Powell (2000), Global three-dimensional MHD simulation of a space weather event: CME formation, interplanetary propagation, and interaction with the magnetosphere, *J. Geophys. Res.*, *105*, 25,053–25,078, doi:10.1029/2000JA900093.

Horbury, T. S., D. Burgess, M. Fränz, and C. J. Owen (2001), Three spacecraft observations of solar wind discontinuities, *Geophys. Res. Lett.*, *28*, 677–680, doi: 10.1029/2000GL000121.

Hundhausen, A. J. (1977), An interplanetary view of coronal holas, in *Coronal Holas and High Speed Streams*, edited by J. B. Zirker, Colorado Associated University Press, Boulder.

Hundhausen, A. J. (1993), The solar wind, in *Introduction to Space Physics*, edited by M. G. Kivelson and C. T. Russell, Cambridge University Press.

Ipavich, F. M., A. B. Galvin, S. E. Lasley, J. A. Paquette, S. Hefti, K.-U. Reiche, M. A. Coplan, G. Gloeckler, P. Bochsler, D. Hovestadt, H. Grünwaldt, M. Hilchenbach, F. Gliem, W. I. Axford, H. Balsiger, A. Bürgi, J. Geiss, K. C. Hsieh, R. Kallenbach, B. Klecker, M. A. Lee, G. G. Managadze, E. Marsch, E. Möbius, M. Neugebauer, M. Scholer, M. I. Verigin, B. Wilken, and P. Wurz (1998), Solar wind measurements with SOHO: The CELIAS/MTOF proton monitor, *J. Geophys. Res.*, *103*, 17,205–17,214, doi:10.1029/97JA02770.

Jeřáb, M., Z. Němeček, J. Šafránková, K. Jelínek, and J. Měrka (2005), Improved bow shock model with dependence on the IMF strength, *Planet. Space Sci.*, *53*, 85–93, doi: 10.1016/j.pss.2004.09.032.

Jurac, S., J. C. Kasper, J. D. Richardson, and A. J. Lazarus (2002), Geomagnetic disturbances and their relationship to Interplanetary shock parameters, *Geophys. Res. Lett.*, *29*, 101–1.

Kessel, R. L., A. J. Coates, U. Motschmann, and F. M. Neubauer (1994), Shock normal determination for multiple-ion shocks, *J. Geophys. Res.*, *99*, 19,359.

Klimov, S., S. Romanov, E. Amata, J. Blecki, J. Büchner, J. Juchniewicz, J. Rustenbach, P. Triska, L. J. C. Woolliscroft, S. Savin, Y. Afanas'yev, U. de Angelis, U. Auster, G. Bellucci, A. Best, F. Farnik, V. Formisano, P. Gough, R. Grard, V. Grushin, G. Haerendel, V. Ivchenko, V. Korepanov, H. Lehmann, B. Nikutowski, M. Nozdrachev, S. Orsini, M. Parrot, A. Petrukovich, J. L. Rauch, K. Sauer, A. Skalsky, J. Slominski, J. G. Trotignon, J. Vojta, and R. Wronowski (1997), ASPI experiment: measurements of fields and waves on board the INTERBALL-1 spacecraft, *Annales Geophysicae, 15*, 514–527.

Knetter, T., F. M. Neubauer, T. Horbury, and A. Balogh (2003), Discontinuity observations with cluster, *Advances in Space Research, 32*, 543–548, doi:10.1016/S0273-1177(03)00335-1.

Knetter, T., F. M. Neubauer, T. Horbury, and A. Balogh (2004), Four-point discontinuity observations using Cluster magnetic field data: A statistical survey, *J. Geophys. Res., 109*, 6102, doi:10.1029/2003JA010099.

Kokubun, S., T. Yamamoto, M. H. Acuna, K. Hayashi, K. Shiokawa, and H. Kawano (1994), The Geotail magnetic field experiment, *J. Geomagn. Geoelectr., 46*, 7–21.

Koval, A., J. Šafránková, Z. Němeček, and L. Přech (2004), Propagation of interplanetary shocks through the solar wind and magnetosheath, submitted to *Advances in Space Research*.

Koval, A., Z. Němeček, J. Šafránková, K. Jelínek, M. Beránek, G. Zastenker, and N. Shevyrev (2005a), The proposal of a small fast solar wind monitor for the SPECTR-R project, in *Proc. Solar Wind 11 – SOHO 16*, pp. 681–684.

Koval, A., J. Šafránková, and Z. Němeček (2005b), A study of particle flows in hot flow anomalies, *Planet. Space Sci., 53*, 41–52, doi:10.1016/j.pss.2004.09.027.

Koval, A., J. Šafránková, Z. Němeček, L. Přech, A. A. Samsonov, and J. D. Richardson (2005c), Deformation of interplanetary shock fronts in the magnetosheath, *Geophys. Res. Lett., 32*, 15,101, doi:10.1029/2005GL023009.

Koval, A., J. Šafránková, Z. Němeček, A. A. Samsonov, L. Přech, J. D. Richardson, and M. Hayosh (2005d), Interplanetary shock in the magnetosheath: Comparison of experimental data with MHD modeling, submitted to *Geophys. Res. Lett.*

Landau, L. D., and E. M. Lifshitz (1960), *Electrodynamics of continuous media*, Pergamon Press.

Lepping, R. P. (1972), Influence of thermal anisotropy on best-fit estimates of shock normals, *J. Geophys. Res., 77*, 2957.

Lepping, R. P., and P. D. Argentiero (1971), Single spacecraft method of estimating shock normals, *J. Geophys. Res., 76*, 4349–4359.

Lepping, R. P., and K. W. Benhannon (1980), Magnetic field directional discontinuities. 2: Characteristics between 0.46 and 1.0 AU, *NASA STI/Recon Technical Report N, 81*, 12,963.

Lepping, R. P., M. H. Acuna, L. F. Burlaga, W. M. Farrell, J. A. Slavin, K. H. Schatten, F. Mariani, N. F. Ness, F. M. Neubauer, Y. C. Whang, J. B. Byrnes, R. S. Kennon, P. V. Panetta, J. Scheifele, and E. M. Worley (1995), The Wind Magnetic Field Investigation, *Space Science Reviews, 71*, 207–229.

Lin, R. P., K. A. Anderson, S. Ashford, C. Carlson, D. Curtis, R. Ergun, D. Larson, J. McFadden, M. McCarthy, G. K. Parks, H. Reme, J. M. Bosqued, J. Coutelier, F. Cotin, C. D'Uston, K.-P. Wenzel, T. R. Sanderson, J. Henrion, J. C. Ronnet, and G. Paschmann (1995), A Three-Dimensional Plasma and Energetic Particle Investigation for the Wind Spacecraft, *Space Science Reviews*, *71*, 125–153.

Lin, Y. (1997), Generation of anomalous flows near the bow shock by its interaction with interplanetary discontinuities, *J. Geophys. Res.*, *102*, 24,265–24,282, doi: 10.1029/97JA01989.

Lindsay, G. M., C. T. Russell, J. G. Luhmann, and P. Gazis (1994), On the sources of interplanetary shocks at 0.72 AU, *J. Geophys. Res.*, *99*, 11–17.

Lucek, E. A., T. S. Horbury, A. Balogh, I. Dandouras, and H. Rème (2004), Cluster observations of hot flow anomalies, *Journal of Geophysical Research (Space Physics)*, *109*, 6207–+, doi:10.1029/2003JA010016.

Luhmann, J. G. (1995), Sources of interplanetary shocks, *Advances in Space Research*, *15*, 355–364.

McComas, D. J., S. J. Bame, P. Barker, W. C. Feldman, J. L. Phillips, P. Riley, and J. W. Griffee (1998a), Solar Wind Electron Proton Alpha Monitor (SWEPAM) for the Advanced Composition Explorer, *Space Science Reviews*, *86*, 563–612.

McComas, D. J., S. J. Bame, B. L. Barraclough, W. C. Feldman, H. O. Funsten, J. T. Gosling, P. Riley, R. Skoug, A. Balogh, R. Forsyth, B. E. Goldstein, and M. Neugebauer (1998b), Ulysses' return to the slow solar wind, *Geophys. Res. Lett.*, *25*, 1–4, doi:10.1029/97GL03444.

Merka, J., A. Szabo, T. W. Narock, J. H. King, K. I. Paularena, and J. D. Richardson (2003), A comparison of IMP 8 observed bow shock positions with model predictions, *Journal of Geophysical Research (Space Physics)*, *108*, 6–1, doi: 10.1029/2002JA009384.

Neubauer, F. M. (1970), Jump relations for shocks in an anisotropic magnetized plasmas, *Z. Physik*, *237*, 205–223.

Neugebauer, M., D. R. Clay, B. E. Goldstein, B. T. Tsurutani, and R. D. Zwickl (1984), A reexamination of rotational and tangential discontinuities in the solar wind, *J. Geophys. Res.*, *89*, 5395–5408.

Newbury, J. A. (2000), Plasma heating and thermal transport in the solar wind near 1 AU, *Ph.D. Thesis*.

Němeček, Z., and J. Šafránková (1991), The Earth's bow shock and magnetopause position as a result of the solar wind–magnetosphere interaction, *J. Atmos. Terr. Phys.*, *53*, 1049–1054.

Nozdrachev, M. N., A. A. Skalsky, V. A. Styazhkin, and V. G. Petrov (1998), Some Results of Magnetic Field Measurements by the FM-3I Flux-Gate Instrument Onboard the INTERBALL-1 Spacecraft, *Cosmic Research*, *36*, 251.

Ogilvie, K. W., D. J. Chornay, R. J. Fritzenreiter, F. Hunsaker, J. Keller, J. Lobell, G. Miller, J. D. Scudder, E. C. Sittler, R. B. Torbert, D. Bodet, G. Needell, A. J. Lazarus, J. T. Steinberg, J. H. Tappan, A. Mavretic, and E. Gergin (1995), SWE, A Comprehensive Plasma Instrument for the Wind Spacecraft, *Space Science Reviews*, *71*, 55–77.

Onsager, T. G., M. F. Thomsen, J. T. Gosling, and S. J. Bame (1990), Observational test of a hot flow anomaly formation mechanism, *J. Geophys. Res.*, *95*, 11,967–11,974.

Parker, E. N. (1958), Dynamics of the Interplanetary Gas and Magnetic Fields., *Astrophys. J.*, *128*, 664.

Parker, E. N. (1963), *Interplanetary dynamical processes.*, New York, Interscience Publishers, 1963.

Paschmann, G., G. Haerendel, N. Sckopke, E. Moebius, and H. Luehr (1988), Three-dimensional plasma structures with anomalous flow directions near the earth's bow shock, *J. Geophys. Res.*, *93*, 11,279–11,294.

Peredo, M., J. A. Slavin, E. Mazur, and S. A. Curtis (1995), Three-dimensional position and shape of the bow shock and their variation with Alfvenic, sonic and magnetosonic Mach numbers and interplanetary magnetic field orientation, *J. Geophys. Res.*, *100*, 7907–7916.

Petrinec, S. M., and C. T. Russell (1996), Near-Earth magnetotail shape and size as determined from the magnetopause flaring angle, *J. Geophys. Res.*, *101*, 137–152, doi: 10.1029/95JA02834.

Petrinec, S. P., P. Song, and C. T. Russell (1991), Solar cycle variations in the size and shape of the magnetopause, *J. Geophys. Res.*, *96*, 7893–7896.

Pizzo, V. J. (1985), Interplanetary shocks on the large scale — A retrospective on the last decade's theoretical efforts, *Washington DC American Geophysical Union Geophysical Monograph Series*, *35*, 51–68.

Russell, C. T., M. M. Mellott, E. J. Smith, and J. H. King (1983), Multiple spacecraft observations of interplanetary shocks Four spacecraft determination of shock normals, *J. Geophys. Res.*, *88*, 4739–4748.

Russell, C. T., Y. L. Wang, J. Raeder, R. L. Tokar, C. W. Smith, K. W. Ogilvie, A. J. Lazarus, R. P. Lepping, A. Szabo, H. Kawano, T. Mukai, S. Savin, Y. I. Yermolaev, X.-Y. Zhou, and B. T. Tsurutani (2000), The interplanetary shock of September 24, 1998: Arrival at Earth, *J. Geophys. Res.*, *105*, 25,143–25,154, doi:10.1029/2000JA900070.

Samsonov, A. A. (2005), Numerical modeling of the Earth's magnetosheath for different IMF orientations, *Advances in Space Research*, doi:10.1016/j.asr.2005.06.009.

Samsonov, A. A., and D. Hubert (2004), Steady state slow shock inside the Earth's magnetosheath: To be or not to be? 2. Numerical three-dimensional MHD modeling, *J. Geophys. Res.*, *109*, 1218, doi:10.1029/2003JA010006.

Schwartz, S. J. (1995), Hot flow anomalies near the Earth's bow shock, *Advances in Space Research*, *15*, 107–116.

Schwartz, S. J., C. P. Chaloner, D. S. Hall, P. J. Christiansen, and A. D. Johnstones (1985), An active current sheet in the solar wind, *Nature*, *318*, 269–271.

Schwartz, S. J., R. L. Kessel, C. C. Brown, L. J. C. Woolliscroft, and M. W. Dunlop (1988), Active current sheets near the earth's bow shock, *J. Geophys. Res.*, *93*, 11,295–11,310.

Schwartz, S. J., G. Paschmann, N. Sckopke, T. M. Bauer, M. Dunlop, A. N. Fazakerley, and M. F. Thomsen (2000), Conditions for the formation of hot flow anomalies at Earth's bow shock, *J. Geophys. Res.*, *105*, 12,639–12,650, doi:10.1029/1999JA000320.

Shue, J.-H., P. Song, C. T. Russell, J. T. Steinberg, J. K. Chao, G. Zastenker, O. L. Vaisberg, S. Kokubun, H. J. Singer, T. R. Detman, and H. Kawano (1998), Magnetopause location under extreme solar wind conditions, *J. Geophys. Res.*, *103*, 17,691–17,700, doi:10.1029/98JA01103.

Sibeck, D. G., N. L. Borodkova, S. J. Schwartz, C. J. Owen, R. Kessel, S. Kokubun, R. P. Lepping, R. Lin, K. Liou, H. Lühr, R. W. McEntire, C.-I. Meng, T. Mukai, Z. Nemecek, G. Parks, T. D. Phan, S. A. Romanov, J. Safrankova, J.-A. Sauvaud, H. J. Singer, S. I. Solovyev, A. Szabo, K. Takahashi, D. J. Williams, K. Yumoto, and G. N. Zastenker (1999), Comprehensive study of the magnetospheric response to a hot flow anomaly, *J. Geophys. Res.*, *104*, 4577–4594, doi:10.1029/1998JA900021.

Sibeck, D. G., T.-D. Phan, R. Lin, R. P. Lepping, and A. Szabo (2002), Wind observations of foreshock cavities: A case study, *Journal of Geophysical Research (Space Physics)*, *107*, 4–1, doi:10.1029/2001JA007539.

Smith, C. W., J. L'Heureux, N. F. Ness, M. H. Acuña, L. F. Burlaga, and J. Scheifele (1998), The ACE Magnetic Fields Experiment, *Space Science Reviews*, *86*, 613–632.

Smith, E. J. (1973), Identification of interplanetary tangential and rotational discontinuities, *J. Geophys. Res.*, *78*, 2054–2063.

Spreiter, J. R., and S. S. Stahara (1992), Computer modeling of solar wind interaction with Venus and Mars, *Washington DC American Geophysical Union Geophysical Monograph Series*, *66*, 345–383.

Spreiter, J. R., A. L. Summers, and A. Y. Alksne (1966), Hydromagnetic flow around the magnetosphere, *Planet. Space Sci.*, *14*, 223.

Stahara, S. S. (2002), Adventures in the magnetosheath: two decades of modeling and planetary applications of the Spreiter magnetosheath model, *Planet. Space Sci.*, *50*, 421–442.

Szabo, A. (1994), An improved solution to the 'Rankine-Hugoniot' problem, *J. Geophys. Res.*, *99*, 14,737.

Szabo, A. (2004), Interplanetary discontinuities and shocks in the Earths magnetosheath, in *Multiscale Processes in the Earths Magnetosphere: From Interball to Cluster,*, edited by J.-A. Sauvaud and Z. Nemecek, pp. 57–71.

Szabo, A. (2005), Determination of interplanetary shock characteristics, in *Proc. Solar Wind 11 – SOHO 16*, pp. 449–452.

Szabo, A., C. W. Smith, and R. M. Skough (2000), The transition of interplanetary shocks through the magnetosheath, *EOS Supp.*, *81*, F966.

Szabo, A., R. P. Lepping, J. Merka, C. W. Smith, and R. M. Skoug (2001), The evolution of interplanetary shocks driven by magnetic clouds, in *ESA SP-493: Solar encounter. Proceedings of the First Solar Orbiter Workshop*, pp. 383–387.

Szabo, A., C. W. Smith, and R. M. Skoug (2003), The Transition of Interplanetary Shocks through the Magnetosheath, in *AIP Conf. Proc. 679: Solar Wind Ten*, pp. 782–785.

Šafránková, J., G. Zastenker, A. Fedorov, Z. Němeček, M. Simersky, O. Vaisberg, L. Přech, Y. Sharko, T. Romasenko, A. Leibov, M. Richter, T. Lesina, N. Plusnina, and Y. N. (1995), Omnidirectional plasma sensor VDP, in *INTERBALL Mission and Payload*, edited by Y. Galperin, p. 195, CNES–IKI–RSA.

Šafránková, J., G. Zastenker, Z. Němeček, A. Fedorov, M. Simersky, and L. Přech (1997), Small scale observation of magnetopause motion: preliminary results of the INTERBALL project, *Annales Geophysicae*, *15*, 562–569.

Šafránková, J., Z. Němeček, L. Přech, G. Zastenker, K. I. Paularena, N. Nikolaeva, M. Nozdrachev, A. Skalsky, and T. Mukai (1998), The January 10-11, 1997 magnetic cloud: Multipoint measurements, *Geophys. Res. Lett.*, *25*, 2549–2552, doi: 10.1029/98GL50330.

Šafránková, J., Z. Němeček, and M. Borák (1999a), MAGION-4 observations of the bow shock crossings, *Czech. J. Phys.*, *49*, 563–578.

Šafránková, J., Z. Němeček, and M. Borák (1999b), Bow shock position: observations and models, in *Interball in the ISTP Program, Studies of the Solar Wind–Magnetosphere–Ionosphere Interaction, NATO Science Series C*, vol. 537, edited by D. G. Sibeck and K. Kudela, pp. 187–202.

Šafránková, J., L. Přech, Z. Němeček, D. G. Sibeck, and T. Mukai (2000), Magnetosheath response to the interplanetary magnetic field tangential discontinuity, *J. Geophys. Res.*, *105*, 25,113–25,122, doi:10.1029/1999JA000435.

Šafránková, J., L. Přech, Z. Němeček, and D. Sibeck (2002), The structure of hot flow anomalies in the magnetosheath, *Advances in Space Research, 30*, 2737–2744.

Thomas, V. A., D. Winske, M. F. Thomsen, and T. G. Onsager (1991), Hybrid simulation of the formation of a hot flow anomaly, *J. Geophys. Res.*, *96*, 11,625.

Thomsen, M. F., J. T. Gosling, S. A. Fuselier, S. J. Bame, and C. T. Russell (1986), Hot, diamagnetic cavities upstream from the earth's bow shock, *J. Geophys. Res.*, *91*, 2961–2973.

Thomsen, M. F., J. T. Gosling, S. J. Bame, K. B. Quest, and C. T. Russell (1988), On the origin of hot diamagnetic cavities near the earth's bow shock, *J. Geophys. Res.*, *93*, 11,311–11,325.

Tsurutani, B. T., and W. D. Gonzalez (1998), Magnetic Storms, in *From the Sun, Auroras, Magnetic Storms, Solar Flares, Cosmic Rays*, p. 57.

Tsurutani, B. T., W. D. Gonzalez, A. L. C. Gonzalez, F. Tang, J. K. Arballo, and M. Okada (1995), Interplanetary origin of geomagnetic activity in the declining phase of the solar cycle, *J. Geophys. Res.*, *100*, 21,717–21,734, doi:10.1029/95JA01476.

Vaisberg, O. L., J. H. Waite, L. A. Avanov, V. N. Smirnov, D. L. Dempsey, J. L. Burch, and A. A. Skalsky (1999), HFA-Like Signatures Observed with the Interball-Tail Spacecraft, in *American Institute of Physics Conference Series*, p. 551.

Viñas, A. F., and J. D. Scudder (1986), Fast and optimal solution to the 'Rankine-Hugoniot problem', *J. Geophys. Res.*, *91*, 39–58.

Villante, U., S. Lepidi, P. Francia, and T. Bruno (2004), Some aspects of the interaction of interplanetary shocks with the Earth's magnetosphere: an estimate of the propagation time through the magnetosheath, *J. Atmosph. Sol.-Terr. Phys.*, *66*, 337.

Whang, Y. C. (1991), Shock interactions in the outer heliosphere, *Space Science Reviews*, *57*, 339–388.

Yan, M., and L. C. Lee (1996), Interaction of interplanetary shocks and rotational discontinuities with the Earth's bow shock, *J. Geophys. Res.*, *101*, 4835–4848, doi: 10.1029/95JA02976.

Zastenker, G. N., A. O. Fedorov, Y. V. Sharko, K. A. Moldosanov, P. A. Dalin, I. P. Kirpichev, L. S. Kim, and M. A. Samsonov (2000), Peculiarities of Usage of Integral Faraday Cups aboard the INTERBALL-1 Satellite: Reduction of Photocurrent and Determination of Incoming Angles and Velocities of Ion Flux in the Solar Wind and the Magnetosheath, *Cosmological Research*, *38*, 20.

Zhuang, H. C., and C. T. Russell (1981), An analytic treatment of the structure of the bow shock and magnetosheath, *J. Geophys. Res.*, *86*, 2191–2205.

Zhuang, H. C., C. T. Russell, E. J. Smith, and J. T. Gosling (1981), Three-dimensional interaction of interplanetary shock waves with the bow shock and magnetopause — A comparison of theory with ISEE observations, *J. Geophys. Res.*, *86*, 5590–5600.

Appendices

A1: Koval, A., Z. Němeček, J. Šafránková, K. Jelínek, M. Beránek, G. Zastenker, and N. Shevyrev (2005), The proposal of a small fast solar wind monitor for the SPECTR-R project, in *Proc. Solar Wind 11 – SOHO 16*, pp. 681–684.

A2: Koval, A., J. Šafránková, and Z. Němeček (2005), A study of particle flows in hot flow anomalies, *Planet. Space Sci., 53*, 41–52, doi:10.1016/j.pss.2004.09.027.

A3: Koval, A., J. Šafránková, Z. Němeček, and L. Přech (2004), Propagation of interplanetary shocks through the solar wind and magnetosheath, submitted to *Advances in Space Research*.

A4: Koval, A., J. Šafránková, Z. Němeček, L. Přech, A. A. Samsonov, and J. D. Richardson (2005), Deformation of interplanetary shock fronts in the magnetosheath, *Geophys. Res. Lett., 32*, 15,101, doi:10.1029/2005GL023009.

A5: Koval, A., J. Šafránková, Z. Němeček, A. A. Samsonov, L. Přech, J. D. Richardson, and M. Hayosh (2005), Interplanetary shock in the magnetosheath: Comparison of experimental data with MHD modeling, submitted to *Geophys. Res. Lett.*